Superlens-assisted anti-counterfeiting Laser Dot Code marking

Wai Hei (William) Kwok

PRIFYSGOL
BANGOR
UNIVERSITY

School of Computer Science and Electronic Engineering
College of Physical and Applied Sciences

Submitted in partial satisfaction of the requirements for the
Degree of Bachelor of Engineering in Electronic Engineering.

Supervisor Dr Zengbo Wang

18th January 2023

Declaration

I hereby declare that this thesis is the results of my own investigations, except where otherwise stated. All other sources are acknowledged by bibliographic references. This work has not previously been accepted in substance for any degree and is not being concurrently submitted in candidature for any degree unless, as agreed by the University, for approved dual awards.

Yr wyf drwy hyn yn datgan mai canlyniad fy ymchwil fy hun yw'r thesis hwn, ac eithrio lle nodir yn wahanol. Caiff ffynonellau eraill eu cydnabod gan droednodiadau yn rhoi cyfeiriadau eglur. Nid yw sylwedd y gwaith hwn wedi cael ei dderbyn o'r blaen ar gyfer unrhyw radd, ac nid yw'n cael ei gyflwyno ar yr un pryd mewn ymgeisiaeth am unrhyw radd oni bai ei fod, fel y cytunwyd gan y Brifysgol, am gymwysterau deuol cymeradwy.
Student:

Wai Hei (William) Kwok

Statement of Availability

I hereby acknowledge the availability of any part of this report for viewing, photocopying or incorporation into future studies, providing that full reference is given to the origins of any information contained herein.

Student:

Wai Hei (William) Kwok

Contents

List of Figures

Acknowledgements

I would first like to thank my thesis advisor Dr Zengbo Wang and Dr. Liyang Yue of the School of Computer Science and Electronic Engineering and the funding of the project from the funding body KESS 2 and Light Future Ltd for funding this project.

The door to both Dr Zengbo Wang and Dr Liyang Yue's office was always open whenever I ran into a trouble spot or had a question about my research or writing. They have consistently provided constructive feedback to steered me towards the right the direction to the completion of the project.

I would also like to thank, Dr Bing Yan who were involved in training of the laser systems, using SolidWorks CAD software to 3D print extension of the motorised stage, and sharing his expertise for his previous research in superlens microscopy and laser material processing with me. Without his passionate participation and input, the necessary skills to complete this project could not have been developed.

I would also like to thank the staff at Aberystwyth University, Dr John Tomes, Mr Simon Astley, Miss Line Macaire, Mr Matthew Wayne Jevon and Mr Alan Cookson who has allowed the use of their facilities to obtain the AFM and SEM data for this project. Without their passionate participation and work ethic over the brief visit to AU, the experimental results could not have been successfully verified.

I would also like to acknowledge Dr John Thomas Prabhakar and Ben Assinder within the department, also for their help with their SEM and AFM microscopy machine respectively.

Finally, I must express my very profound gratitude to my parents and to my girlfriend Jennifer for providing me with unfailing support and continuous encouragement throughout my years of study and through the process of researching and writing this thesis. This accomplishment would not have been possible without them. Thank you.

Abstract

Counterfeiting is a global issue and has considerable negative impacts on our society, both economically and socially. Existing anti-counterfeiting methods such as watermarks, holograms, and conventional laser marking are, however, becoming old-dated and ineffective. This project aims to develop a new laser-based anti-counterfeiting technology – *Superlens-assisted anti-counterfeiting Laser Dot Code marking* – which can effectively prevent and detect counterfeiting, and difficult to be copied by counterfeits. This project is timely and of considerable potential social and economic impacts to Wales, the UK and internationally.

The key concepts behind the project include: (1) Using DotCode scheme in laser marking to replace TEXT or other 2D code schemes (e.g QR code) for enhanced security; (2) integrating particle superlens array into laser dotcode marking process to reduce laser focus spot size from microscale to nanoscale. Such nanofeature-decorated DotCode marking is unique and hardly to be copied.

Experimentally, we first performed direct laser marking of dotcode on stainless and glass surface without particle superlens by using UV and femtosecond (FS) lasers. Advantages of DotCode scheme over other 2D codes were demonstrated, including higher manufacturing speed, better scalability, and readability. It is also shown that FS laser has clear advantages over UV lasers in DotCode marking in terms of marking quality and feature size. However, driven by the commercial needs on low-cost solution, the superlens-assisted marking was explored using UV laser only. To deposit a large-area monolayer of microsphere array on glass surface, three different techniques were tried, including drop-casting, spin-coating and Modified Langmuir-Schaefer (MLS) techniques. The MLS technique was chosen for the project due to its ability to generate required large-area monolayer particle arrays. A group of different UV laser fluences were then tested, with the aim to find best laser parameter window for the marking process. After this, the readout of laser-marked nano DotCode were tried with Scanner App. The laser-marked nano Dot Codes are completely invisible to human eyes and can only be revealed by microscopic imaging followed by image processing. Theoretical calculation of particle superlens focusing was also carried out to support the experiments. As

a result, the proposed technique successfully demonstrates its unique ability in protecting the information being counterfeited by others.

Chapter 1

INTRODUCTION

1.1 Anti-counterfeiting

As new opportunities open up on with globalisation and the accessibility of the internet, it is important for many industries to acknowledge the threat of IP (Intellectual property) crime and equip its products with suitable anti-counterfeiting technologies to prevent business owners and customers from falling victim to IP crime. The harm caused by IP crime impacts not only company profits and tax revenue, it extends to threatening global public health safety with the most recent cases involving fake COVID-19 vaccines being distributed among the global population [1].

Laser marked codes has been used as an effective tool in anti-counterfeiting applications [2]–[5]. Laser marked codes are difficult to rubbed off in comparison to ink-based codes, making them the ideal solution for traceability and anti-counterfeiting: laser marking creates a permanent, indelible mark. Distinct 2D codes, such as QR code, Data Matrix code and DotCode, can help create additional level of security and complexity to deter counterfeiters.

However, due to rapid growth of laser technology especially the fiber laser technology, the prices for conventional laser marking systems drop considerably in recent years and a low-end marking system now only costs less than £2k, making it accessible to more and more people and also the counterfeiters. We thus need new innovations to improve the security level of our markings so that a counterfeiter with a laser marking system cannot copy or reproduce our markings.

For this, we advocate to use the Dot Code scheme in marking to improve the security level. On top of this, a second level of security will be added by integrating superlens into the marking process to reduce each individual marking size from micro to nano (see **Figure 1.1**). As a result, information will be encoded in a 2D Dot Code marking where each dot among

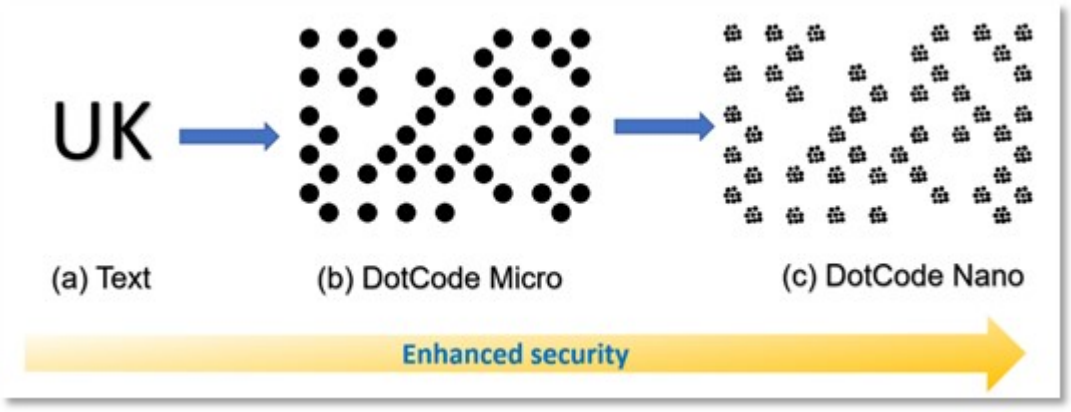

Figure 1.1 – Project concept. Evolution from (a) conventional laser text marking to (b) dot code micro marking and further to (c) dotcode nano marking assisted by superlens.

the Dot Code is made of several nanoscale holes. Such two-level security features make our 2D Dot Code more difficult to be replicated by other counterfeiters and thus provides an effective anti-counterfeiting solution for protection of authentic products such as diamonds and jewelries.

1.2 Aims and Objectives

The project aims to develop a superlens-assisted DotCode Laser Marking (SDCLM) technology for high-level anti-counterfeiting applications. The generated DotCodes by developed SDCLM technique are highly-secure: they are almost 'invisible' to the overserves, and contains distinct signature nanoholes within each marking dot hardly to be counterfeited. The objectives of the project are to:

- Generate DotCodes on various samples by direct laser marking method, and compare with other methods (text, QR codes)
- Develop a method to deposit superlens array on sample surface for nanoscale marking.
- Demonstrate two-level security marking by proposed SDCLM technology and successful readout.
- Explore super-resolution mechanism associated with particle superlens.

1.3 Thesis Outline

Chapter 2 reviews some current anti-counterfeiting techniques available on the market, the operating principles of lasers and the light-matter interaction in laser materials processing, the theoretical methods of light focusing to achieve super-resolution and the methods of

fabricating an HCP (Hexagonal Close Packed) self-assembled monolayer for use in laser materials processing.

Chapter 3 details the experimental setups for the laser marking and sample characterization, and the preparation procedures for the substrate and colloidal microspheres. Experiments were divided into two sections, 1) Fabricating a large-area high-quality mono-layer suitable for laser marking. 2) Laser Dot Code marking. Theoretical simulation and code recognition software used in the experiment are also detailed.

Chapter 4 details the main results. Firstly, various 2D code markings were compared in terms of manufacturing speed, scalability, and readability. It confirms the advantages of Dot Code scheme over other popular 2D codes. Direct fabrication of Dot Code by UV and femtosecond laser was then compared. Following that, results on monolayer fabrication by three different methods (Drop-casting, Spin-Coating and Modified Langmuir-Schaefer method) were presented and compared. By coupling particle array with UV laser source, tens of laser fluences were used to fabricate the nanoscale Dot Codes. The size and depths of fabricated nanoholes were measured and compared, confirming it subwavelength size scale due to near-field focusing by particle superlens. Readout of nano Dot Code were then reported. At last, modelling and simulation of superlens focusing at different conditions were studied, the theoretical results were used to support and explain the experimental findings which are in good agreement.

Chapter 5 summarizes the whole project and discussed the future work.

Chapter 2

LITERATURE REVIEW

This chapter introduces common anti-counterfeiting techniques, and current existing 2D security codes and highlighting the symbology of each type, followed by introduction to laser fundamentals and the underlying physical phenomena that occurs during laser ablation for material processing.

As well as the introduction of optical diffraction limit (ODL), which restricts the minimum feature size during laser materials processing. Followed by the related literature review of optical super-resolution techniques to overcome the ODL and achieve the resolutions that are below diffraction limit.

Most related to the project, is the **photonic nanojet** phenomena using micro-spheres, super-resolution techniques utilising the photonic nanojet that enabling laser light focusing to sub diffraction limit during material processing. Concluding with reviews of mono-layer fabrication techniques that allow for microspheres to be arranged into an HCP array.

2.1 Anti-counterfeiting technology (ACT)

The European union intellectual property office (EUIPO) published a guide on anti-counterfeiting technologies (ACT) [6]. It provides an overview of the various solutions currently available and sets the groundwork for building an anti-counterfeiting strategy. It includes following categories:

- Electronic technologies – RFID (radio-frequency identification), NFC (near-field communication) devices, electronic seals, Magnetic stripes, contact chips.
- Marking technologies – Text, Watermarks, holograms, inks, Encrypted images, Rainbow printing, unique identifier marks, copy detection patterns, Optical memory strip, machine-readable codes etc. (See **Figure 2.1**)

- Mechanical technologies – Labels, Laser engraving, anti-alteration devices, seals, security threads, security films.
- Digital media technologies – DRM (digital rights management) systems, Digital watermarks, Hashing, Fingerprinting
- Shared Ledger Technology -Blockchain

The ISO 22383:2020 provides guidance for organisations on how to go about selecting the most appropriate 'authentication elements' (devices used as part of an authentication solution) to validate the authenticity of their material goods and sets out criteria that can be used to analyse and compare different options. This Standard does not prescribe any one exclusive means of authentication. This project aims to develop a new laser-based anti-

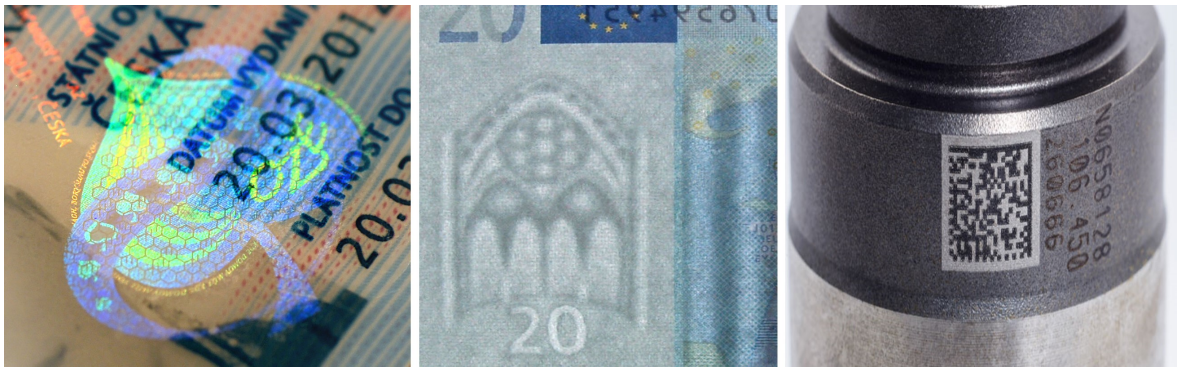

Figure 2.1 – Example of anti-counterfeit technologies. (a) Hologram (b) watermark (c) laser marking

counterfeiting technology which fall within marking and mechanical technology categories listed above. However, our technique builds upon novel concept of combining laser marking with particle superlens and dotcode scheme which haven't been explored in the literature. In the following, we will focus on the 2D code schemes used in laser marking, fundamentals of laser marking, superlens and microsphere-assisted nanopatterning including microsphere monolayer formation.

2.2 2D codes

2.2.1 Code-128 Barcode

Figure 2.2 – Code-128 barcode with the encoded message - Bangor University. *Generated with Aspose Pty. Ltd. barcode generator.*

Code 128 was invented in 1981 by Ted Williams of Laserlight Corporation to encode both alphabetic and numeric characters. The Code 128 barcode consists of linear bar as shown in **Figure 2.2**, that encodes all of the 128 ASCII code characters (numbers, upper case/lower case letters, symbols and control codes) typically printed onto products and containers in the shipping and products industries as a product identifier.

Code 128 contains 106 different printed barcode patterns. Each printed barcode may have one of three different meanings depending upon which of the character sets are being used, with the availability of three different Code 128 start characters to program the initial character set. Functions are also provided in the barcode symbology to switch between character sets and encode Application Identifiers.

2.2.2 Data Matrix

The Data Matrix code was invented in 1994, by US company International Data Matrix, Inc. capable of encoding up to 2,335 alphanumeric characters code consisting of black and white cells arranged in as a square or a rectangular pattern as shown in **Figure 2.3**. In the example below, each dark cell corresponds to 1 and white corresponds to 0 with a L-shaped border functioning as a "finder pattern" used to locate and orient the symbol, and the alternating dark and white cells on the opposite side is known as the timing pattern, used to provide a count of the number of rows and columns in the symbol.

The Data Matrix code can be scaled to a large range of sizes, finding applications with track and trace, anti-counterfeiting, in aerospace, electronic, and automotive industries with images as small as 300 μm [7], [8].

(a) An example of Data Matrix code with encoded message "Bangor University"

(b) Reading Data Matrix on mobile phone

(c) Data Matrix on mini PCI card

Figure 2.3 – Examples of Data Matrix code

2.2.3 Aztec code

Aztec code is a public domain 2D barcode invented by Andrew Longacre, Jr. and Robert Hussey in 1995 [9]. Aztec encoding consists of concentric square rings surrounds a bull's-eye pattern. The central bull's eye consists of 9x9 or 13x13 pixels, and the perimeter consists of a row of pixels encoding basic parameters. Data is added on the layer by layer, each layer containing two rings of pixels, for a total size of 15x15, 19x19, 23x23 pixels etc. The corners of the core (See **Figure 2.4 (a)**) includes the orientation markers, allows for the code to be read under rotation or reflection. Beginning at the corner with three black pixels, decoding proceeds clockwise to the corners with two, one, and zero black pixels (See **Figure 2.4 (b) and (c)**). Unlike other bar-codes, it is not necessary for Aztec code to mark the boundary with a blank "quiet zone" since the variable pixels in the central core encode the size, this property of the Aztec code gives it the potential to use fewer space than other matrix codes and has found applications in transport ticketing commonly seen on electronic boarding passes across the transport industry, driver's identification cards in Poland and tax invoices in Russia (See **Figure 2.4 (d)**)

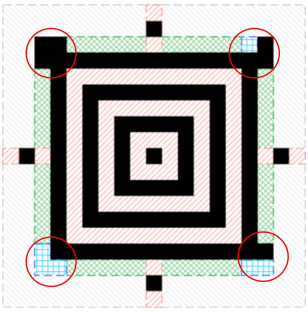

(a) Aztec code core, with the orientation markers circled in red.

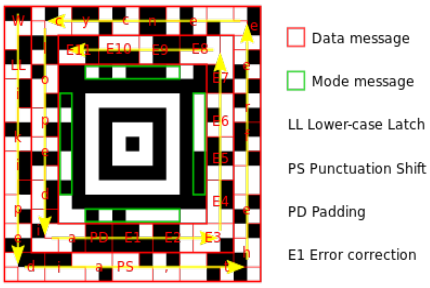

(b) Aztec code structure

(c) Example of Aztec code with the message "Bangor University" encoded.

(d) Polish Driver's license with Aztec code identifier

Figure 2.4 – Demonstrations of the Aztec code structure and applications.

2.2.4 QR code

QR (**Q**uick **R**esponse) code is a type of 2D barcode created in 1994 by Masahiro Hara from the global automotive components company, Denso Wave to create a facile and automatic tracking process of automotive components in the automotive production line [10]. The QR code consists of black squares arranged in a square grid on a white background, which can be read by an imaging device such as a camera and corrected using Reed–Solomon error correction (See **Figure 2.5 (a)**). The QR code encoding occurs in two directions: horizontally and vertically. It can be read easily and is capable of holding a great deal of information (See **Figure 2.5 (c)**). QR codes have become increasingly common in everyday life in recent years, found applications in: payment systems, restaurant ordering, counterfeit detection, electronic authentication by generating time-limited one-time passwords and product tracing [11].

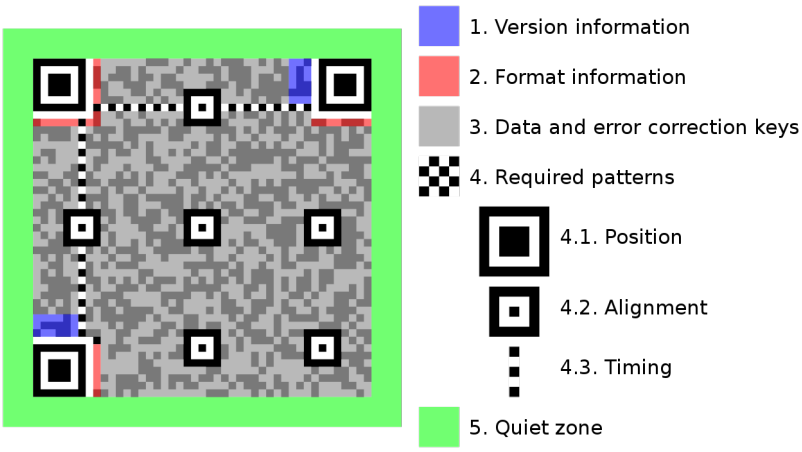

(a) Structure of a QR code

(b) QR code with encoded message Bangor University

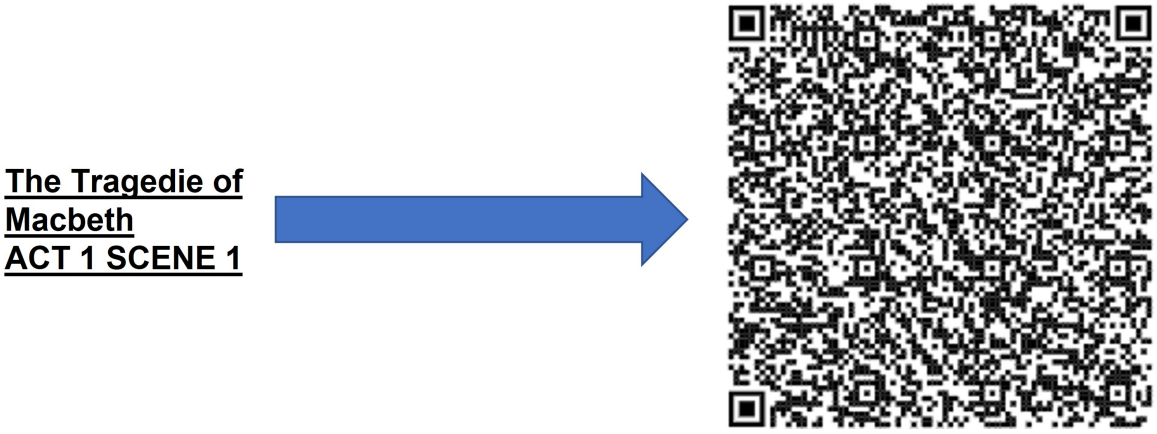

(c) QR code with encoded the act 1 scene 1 of The Tragedie of Macbeth

Figure 2.5 – Figure of the QR code structure and demonstration of the number of information capable to be encoded into a QR code.

2.2.5 Dot code

Dot Code is a public domain 2D barcode symbology composed of disconnected dots, developed by Dr. Andrew Longacre in 2007. Dot Codes are equipped with error correction capabilities using Reed-Solomon correction algorithm , which works to detect and restore missing data in 2D codes[12], [13]. Data in Dot Codes are encoded as 'data dots' which can be circular dots or rectangular shapes, this is beneficial for the project due to the circular dots matching the laser beam shape and thus, additional beam shaping is not required. Dot Codes can be utilized on light or dark colored backgrounds, provided that there is a sufficient contrast between the code and its background. Dot codes can encode data using GS1 data structures (application identifiers + data) as stated in GS1 General Specification. All 128 ASCII characters, i.e., ASCII characters 0 to 127 inclusively, in accordance with ISO 646. [14]. An example of Dot Code is shown in **Figure 2.6**.

Limitations of Dot Code

The minimum size of a Dot code to encode data is 7 dots in each direction, also if one axis contains an odd number of dots then the other must have an even number of dots. Thus, rectangular codes will be generated every time. Although there isn't a theoretical maximum limit for the Dot Code to encode information but, there is a practical limit to how many dots most printing technology can only achieve 124 dots in either direction.

Currently, cigarettes manufacturers are employing a combination of 2D codes such as Dot Code, Data Matrix and OCR (Optical Characters Recognition) on the packaging of a product to allow for the tracking and tracing of the products in the supply chain (**Figure 2.7**)

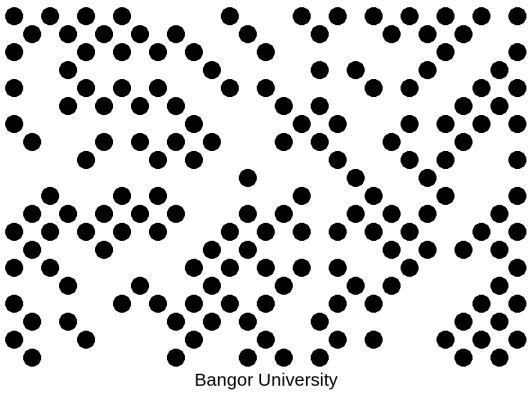

Figure 2.6 – Example of a Dot Code, with "Bangor 2022" encoded.

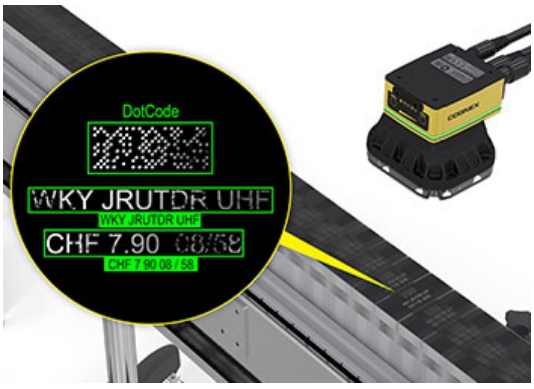

Figure 2.7 – Reading Dotcode and text in a cigarette supply chain.

2.3 Laser material processing fundamentals

The first laser was built by Theodore H. Maiman on 16th May 1960. The term Laser is an acronym for **L**ight **A**mplification by **S**timulated **E**mission of **R**adiation, radiation produced via stimulated emission exhibit three properties, monochromaticity (Single wavelength), coherency (Same phase) and collimation (Low divergence), these three properties allow for lasers to produce highly intense beams with a small focal point. Since then, many different types (solid-state, gas, semiconductor diode lasers and many more) of lasers have developed to utilise these properties to have found applications in many industries such as, security, automotive, medical, telecommunication, electronics and countless others.

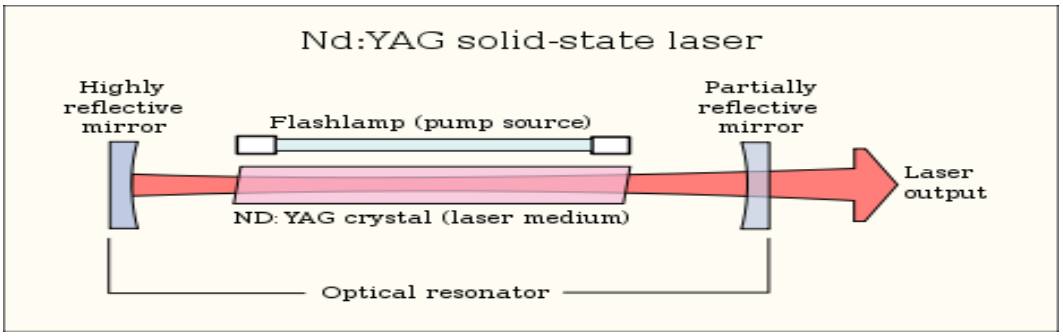

Figure 2.8 – Schematic of a typical Nd:YAG solid-state laser.

2.3.1 Operating Principle of Lasers

In the simplest case, simulated emission occurs within the laser/gain medium of a laser system , where two energy levels of an atom is excited by an incident photon of energy, hν. Interaction with the atomic electron to cause the excited electron at a higher energy state, E_2 to drop to a lower energy state E_1, emitting a photon. The emitted photon are identical to the incident photon in frequency (thus photon energy), phase, directionality and polarisation. As shown in **Figure 2.9**.

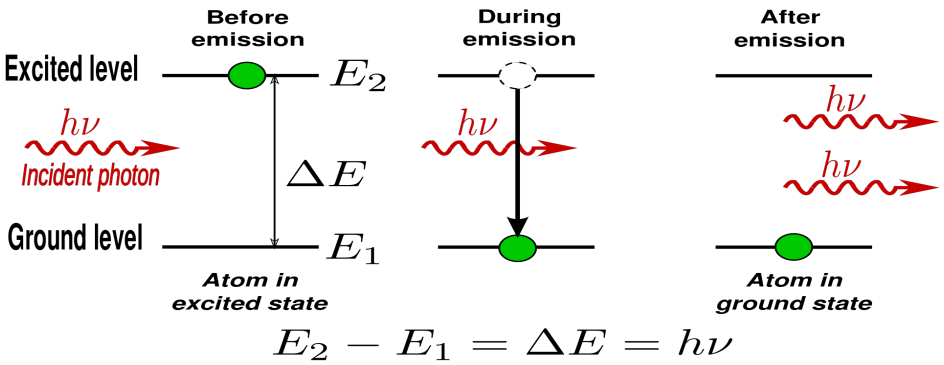

Figure 2.9 – Illustration of two level laser system

2.3.2 Population inversion

Population inversion is achieved when the higher energy states are significantly more populated above 50% than the lower energy states. In two-level system, population inversion is not possible as the rate of absorption and stimulated emission are proportional to the populations in the lower and upper energy levels. Population inversion can be be achieved in a three and four-level system.

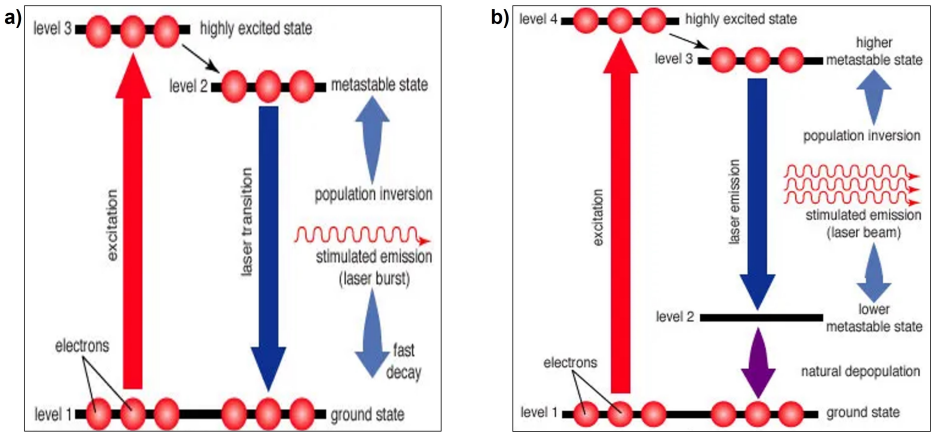

Figure 2.10 – (a) Three level laser system, (b) Four level laser system (Taken from Encyclopedia Britannica inc.)

2.3.3 Three-level laser system and Four-level laser system

Figure 2.10 shows the three and four-level laser system configurations. In a three-level laser system such as the ruby laser made by Theodore H. Maiman, (See **Figure 2.10 a)**), the electrons of the atom are excited/pumped from the ground state (level 1) to a higher energy state (level 3) then spontaneously drops to a lower-energy state (level 2) with an long lifetime essentially holding and trapping the excited electrons on level 2, this results builds up a **population inversion** (Condition in which the population in the higher energy state is higher than the lower states), which can be further stimulated to achieve lasing when the electrons from the meta-stable state drops to the ground state. The issue that arises with a three-level laser system is that the population inversion can only be achieved when the ground state is depopulated, since the lasing occurs from level 2 to the ground state, the electrons accumulates onto the ground state, where absorption occurs preventing stimulated emission and shut down lasing action. Therefore, three-level lasers can only generate pulses.

For continuous wave lasers, this issue is overcome by a transition level between the meta-stable state and ground state (four-level system). Referring to **Figure 2.10 b)**, a four-level laser

system, the lasing action occurs between level 3 and level 2, which maintains the population inversion state between level 3 and the ground state.

2.4 Laser Materials Processing

Laser materials processing involves the application of a laser beam to precisely heat/melt/ vaporise a wide range of materials to carry out material modifications to various applications. In materials processing, lasers has been employed in micro and nanopatterning of materials [15]–[18], cleaning of surfaces from contamination layers and particulates[19], [20], thin film deposition [21] as well as medical applications [22], [23].

The laser light-matter interaction mechanisms during laser processing is determined by the laser parameters and the physical and chemical properties of the target material. The laser parameters are characterized by its wavelength, λ, intensity, I, spatial and temporal coherence, polarization, angle of incidence, dwell time (illumination time at a particular site) and its diffraction-limited Gaussian beam quality, the material is characterized by its chemical composition, crystal structure and the band gap. For example in IR processing, the laser beam excites the free electrons in metals, and vibrations within insulators, semi-conductors can undergoes both excitation regimes depending on its band-gap. The excitation energy inside the irradiated material increases, and dissipates as heat energy thereby, inducing a temperature rise on the surface and into the bulk of the material. **Figure 2.11** shows the effect of laser intensity to the material surface.

In **Figure 2.11a)**, at low/medium intensities, the energy is sufficient to undergo solid to liquid phase transition (**melting** or boil the material). **Figure 2.11b** shows the **sublimation** and **vaporization** phase transition.

2.4.1 Laser Ablation

Laser ablation generally refers to the removal of materials from a solid surface by pulsed laser irradiation, the solid material is heated up by the absorbed laser energy upon laser irradiation, undergoes phase transition. From solid to liquid (Evaporation), solid to gas (Sublimation) and gas to plasma (Ionization) [25].

In the case of laser ablation of metals targets, the laser energy is absorbed by the free electrons, due to inverse Bremsstrahlung. The absorbed energy is transferred to the lattice, and energy

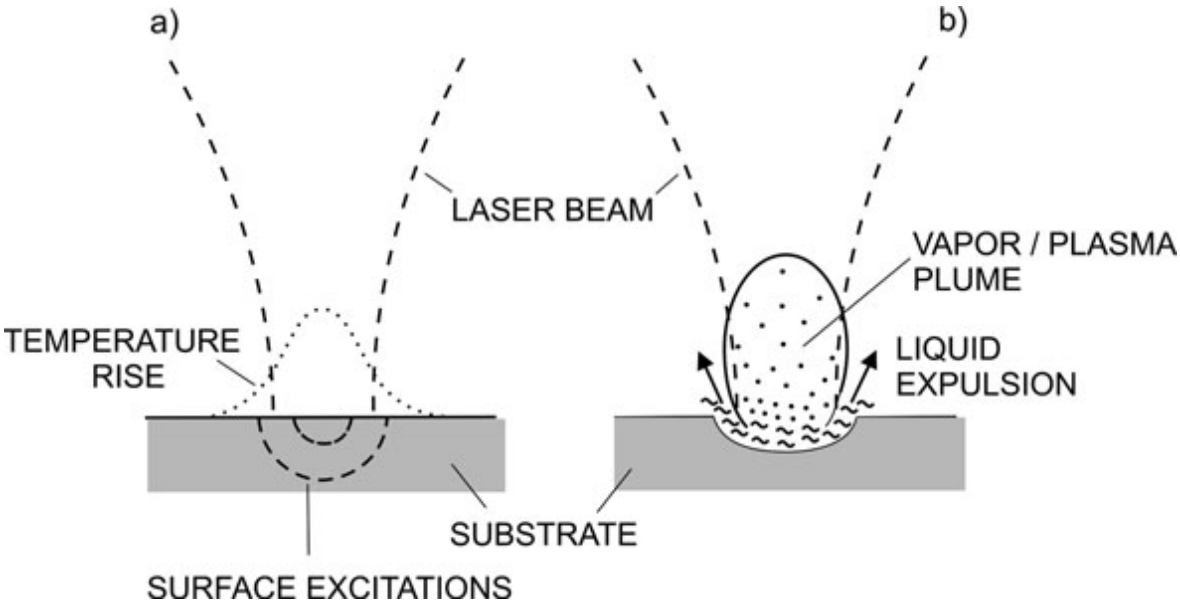

Figure 2.11 – (a) Laser intensity less than vaporization threshold I < I_v (b) Laser intensity greater than vaporization threshold features melting of the material, liquid expulsion and vapor/plasma plume. [24]

losses from electron heat transport into the target. the energy transport into the metal target are described in Equation 2.1 - 2.3 taken from [26].

$$C_e \frac{\partial T_e}{\partial t} = -\frac{\partial Q(z)}{\partial z} - \gamma(T_e - T_i) + S \tag{2.1}$$

$$C_i \frac{\partial T_i}{\partial t} = \gamma(T_e - T_i) \tag{2.2}$$

$$Q(z) = -k_e \frac{\partial T_e}{\partial z}, S = I(t) A \alpha exp(-\alpha z) \tag{2.3}$$

z is the direction perpendicular to the target surface, Q(z) is the heat flux, S is the laser heating source term, I(t) is the laser intensity, A = 1 - R and α are the surface transmissivity and the material absorption coefficient, C_e and C_i are the heat capacities (per unit volume) of the electron and lattice subsystems, γ is the parameter characterizing the electron-lattice coupling, k_e is the electron thermal conductivity. These equations have characteristic timescales, and can be simplified when taking the laser pulse duration relative to the electron cooling time into consideration and fully theoretically described in [26], [27].

Comparison of the characteristics of nano and femtosecond pulses

Numerous studies have been conducted investigating the differences of using different laser duration pulses to process a material [28]–[30]. Laser pulse duration is an important parameter for laser ablation, the physical processes involved are shown in **Figure 2.12**. Notably, in the nanosecond regime, plasma formation occurs during the laser pulse. Therefore the laser pulse reheats the plasma, creating a larger HAZ as shown in **Figure 2.13**, in contrast for the femtosecond laser regime, the plasma formation occurs after the laser pulse has ended, therefore the HAZ is minimal in the femtosecond regime.

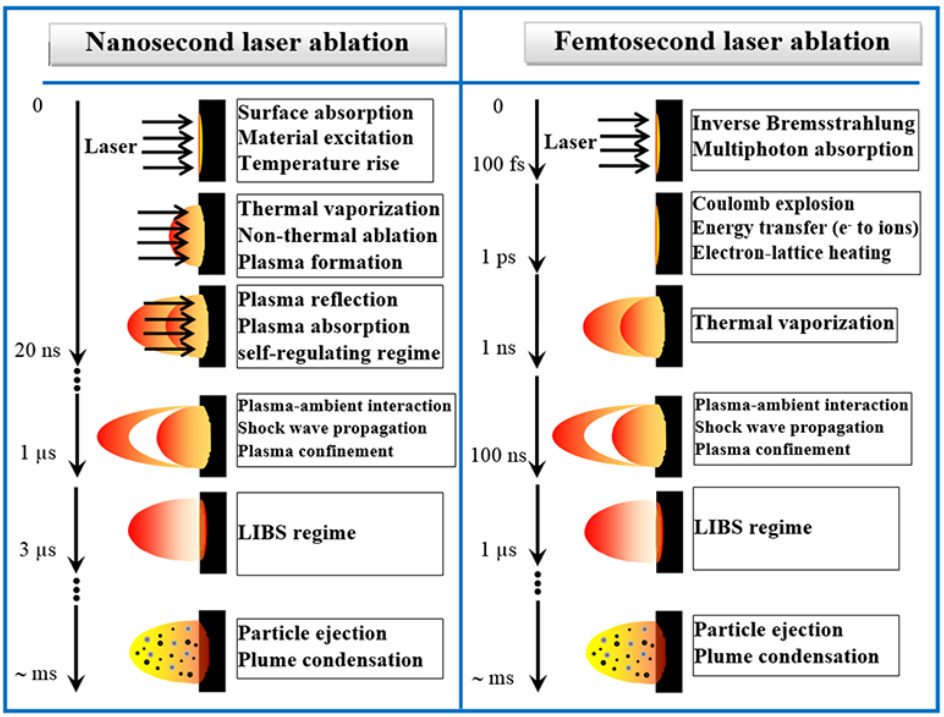

Figure 2.12 – Timescale comparison of physical processes during laser-matter interaction

The experimental results shown in [26] (See **Figure 2.14**) compares different pulse duration to fabricate craters with 100 microns diameter in steel in vacuum (10^{-4} mbar), Laser Ti-sapphire with a) 3.3 ns (4.2 Jcm^{-2}), b) 80 ps (3.7 Jcm^{-2}) and c) 200 fs (0.5 Jcm^{-2}). Evidently, the femtosecond laser created minimal damage to the surrounding material, as the longer pulse duration reheats the plasma, causing vaporization which in turn introduces a recoil pressure expelling materials vertically.

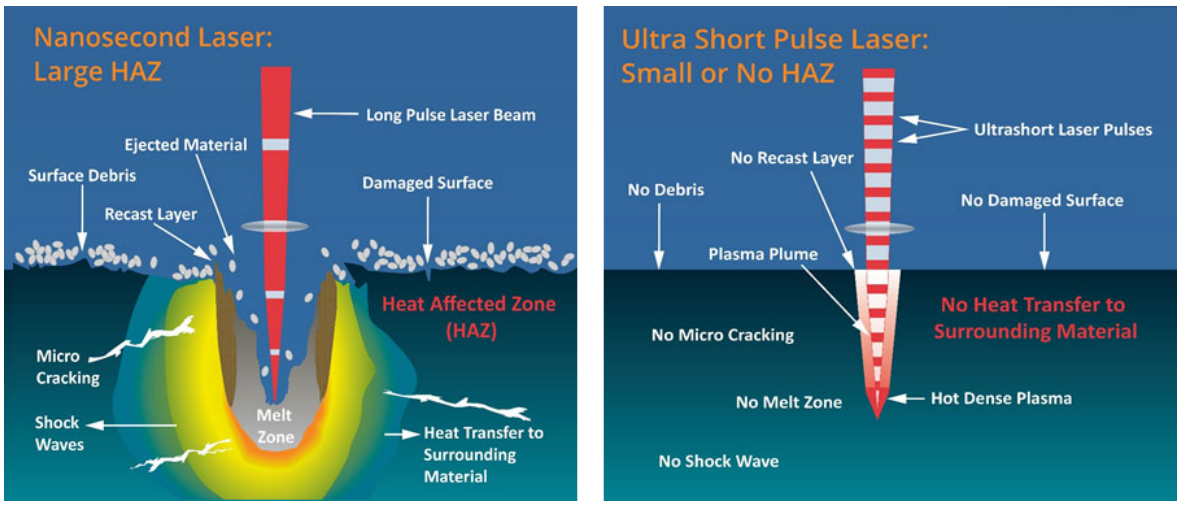

Figure 2.13 – Comparison of size of HAZ and underlying mechanisms in laser processing with nanosecond and femtosecond

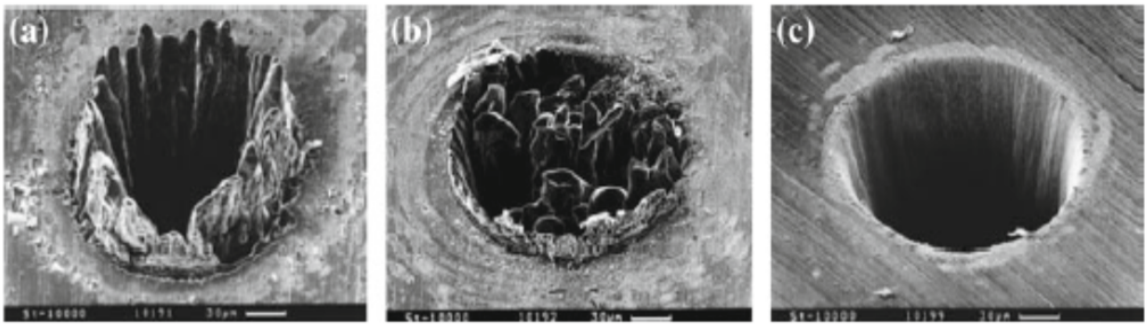

Figure 2.14 – Comparison of laser-drilled craters in the a) 3.3 ns b) 80 ps c) 200 fs regimes.

2.4.2 Mode-locking

Mode-locking is a technique which induces a fixed phase relationship between laser cavity modes. The constructive interference between the fixed phase modes produces a train of intense pulses. Depending on the property of the laser, such as the size and bandwidth, these pulses can be in the order of 10^{-12} to 10^{-15}s (pico- to femto).

Laser cavity modes

Within a laser system, the laser produces light over some natural bandwidth or a small range of frequencies. The first factor of a laser's bandwidth of operation is determined by the gain medium and the laser is constructed from, the range of frequencies that a laser may operate over is known as the gain bandwidth. The second factor affecting the laser's frequency is the resonant cavity of the laser of the laser. For example: the Nd:YAG laser shown in **Figure 2.8**, The resonant cavity consists of two plane mirrors facing each other surrounding the gain medium. Due to the light exhibiting wave-like properties, constructive and destructive

interference with itself occurs, leading to the formation of standing waves between the mirrors. The standing waves form discrete set of frequencies known as a longitudinal modes of the cavity. In a plane-mirror cavity, the requirement for longitudinal modes within a laser cavity is given such that the distance between the mirrors L is an exact multiple of half of the wavelength of light within the cavity, λ. As shown in Equation 2.4. where q is the mode order number integer.

$$L = q\frac{\lambda}{2} \tag{2.4}$$

Moreover, the frequency separation, $\Delta\nu$, between any adjacent modes q and q+1 is given by the Equation 2.5 where c is the speed of light.

$$\Delta\nu = \frac{c}{2L} \tag{2.5}$$

Using Equation 2.5, it is possible to determine the number of longitudinal modes within a laser cavity. For example for a 30 cm cavity, the frequency separation, $\Delta\nu$ is 0.5GHz, for a HeNe laser with 1.5 GHz bandwidth can support 3 longitudinal modes within the cavity and a Ti:Saphhire laser with a 128THz bandwidth can support 2.56×10^5 longitudinal modes.

Each individual longitudinal mode has some bandwidth or narrow range of frequencies it operates, but this is much smaller than the inter-mode frequency separation. In practice, each of the longitudinal modes oscillate independently, emitting laser light in slightly different frequencies. In simple laser systems, individual modes oscillate in the cavity independently, with no fixed relationship between them, for laser systems few longitudinal modes (such as a HeNe laser), the interference between the modes can causes beating effects in the laser output, leading to random fluctuations in intensity; in lasers supporting modes $\gg 10^3$, the interference effects average out to a near-constant output intensity, yielding a continuous wave (CW) laser.

If the modes were oscillating with a fixed phase relationship between them, the laser is said to be mode-locked, the modes periodically all constructively interfere, producing an intense pulse of light. The duration of the pulse is inversely proportional to the number of modes in the cavity. For Gaussian temporal beam shapes the minimum possible pulse duration Δt is given by:

$$\Delta t = \frac{0.44}{N\Delta\nu} \tag{2.6}$$

Where N is the number of modes, the 0.44 is known as the time-bandwidth product determined by the beam shape, for $sech^2$-shaped pulses the time-bandwidth product is approximately 0.315. For the 128THz bandwidth Ti:Sapphire laser, Δt is $\approx$ 3.4 fs.

Mode-locking method - Active mode-locking

There are two main categories of generating femtosecond laser: active mode-locking and passive mode-locking. In active mode-locking, an active element, such as an acousto-optic (AOM) or an electro-optic modulator periodically modulates the cavity loss [31]. The modulator serves two primary functions [32].

• A pulse with the "correct" timing can pass the modulator at times where the losses are at a minimum (see **Figure 2.15**). It is thus favored against any other radiation circulating in the resonator. As the pulse will in the steady state saturate the laser gain such that its round-trip gain is zero, other circulating radiation will have a negative round-trip gain and will thus die out sooner or later.

• The wings of the pulse experience small attenuation, which effectively leads to pulse shortening in each round trip: The round-trip gain is slightly negative for the wings and slightly positive for the pulse center. As a result, the pulses get shorter and shorter, until the pulse shortening is offset by other effects (e.g. gain narrowing or chromatic dispersion) which tend to broaden the pulse

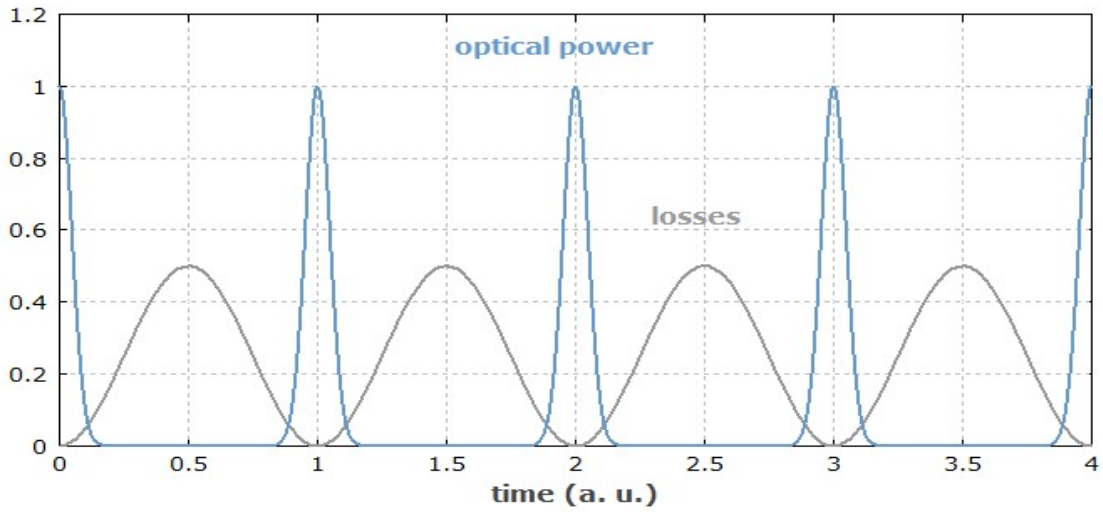

Figure 2.15 – Temporal evolution of optical power and losses in an actively mode-locked laser. The modulator causes increased losses for the pulse wings, effectively shortening the pulses. As the pulse duration relative to the pulse period is typically much smaller than shown, the pulse-shortening effect of the modulator is usually very weak. Taken from [32]

Mode-locking method - Passive mode-locking

In the case of passive mode-locking, this is typically done by incorporating a saturable absorber inside the laser cavity. The most commonly method for passive mode locking is the semiconductor saturable absorber mirror (SESAMs), invented by U.Keller in 1992 [33]. Ideally, a saturable absorber attenuates incident low-intensity light, and transmit light with sufficiently high-intensity light. Each time laser of a high enough intensity hits the saturable absorber, it saturates the absorption, thus reducing the losses as shown in **Figure 2.16** and a net gain value is achieved. Any light of lower intensity which hits the absorber at other times will experience losses which are higher than the gain, since the absorber cannot be saturated by this light. The absorber can thus suppress any additional (weaker) pulses in addition to any continuous background light [34], this selective amplification effect produces a train of pulses of mode-locked laser light, also the leading wing and trailing wings of the circulating pulse are attenuated in a saturable absorber, leading to decrease of pulse duration typically down to femtosecond scale.

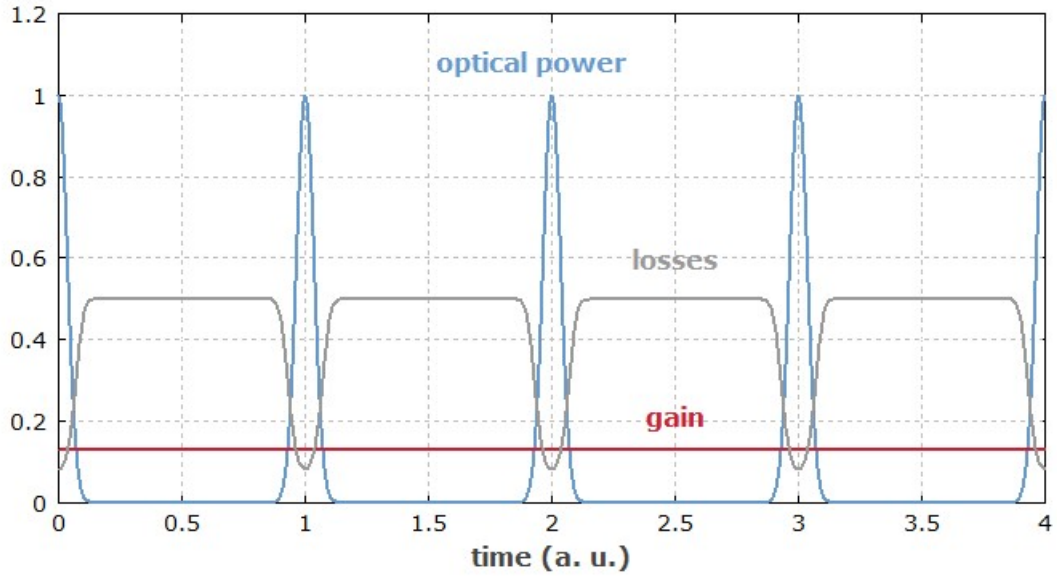

Figure 2.16 – Temporal evolution of optical power and losses in a passively mode-locked laser with a fast saturable absorber. The shorter the pulse becomes, the faster will be the loss modulation. The gain stays approximately constant, as gain saturation is weak. Taken from [34].

2.5 Light focusing and Optical Super-Resolution

2.5.1 Diffraction

Diffraction is an optical phenomenon that occurs when any wave (mechanical, electromagnetic, acoustic etc.) encounters an obstacle or aperture, where its size order of magnitude is comparable to the incident wavelength, resulting an apparent bending and spreading of the waves forming a diffraction pattern, also depending on the distance away from the aperture, different diffraction patterns can be observed these are generally are characterised into three types: (1) Near-field diffraction (2) Fresnel diffraction and (3) Far-field diffraction as shown in **Figure 2.17**. In the region in close proximity after the aperture opening, D, the irradiance

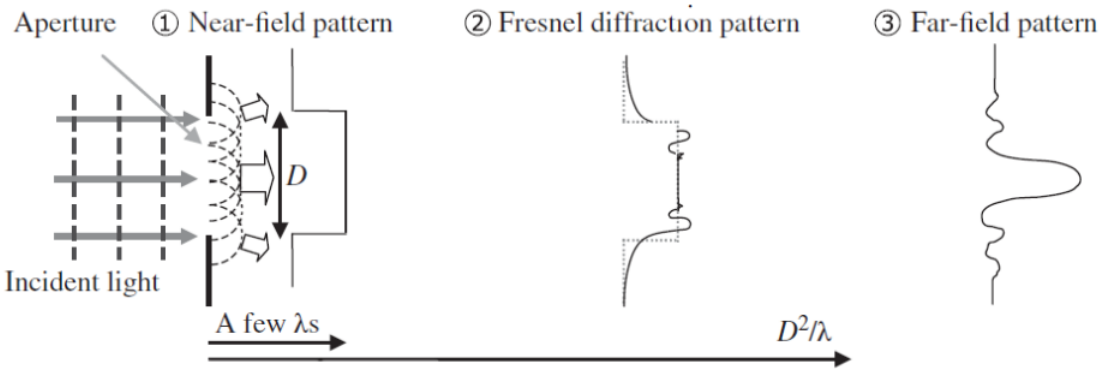

Figure 2.17 – Diffraction patterns observations with increasing axial distance (Z). Taken from [35]

pattern is the shape of the aperture (near-field), as the axial distance increases to 2λ, the Fresnel diffraction pattern is observed, and finally, when the axial distance, z is greater than D^2/λ, the far-field pattern can be observed.

2.5.2 Resolution limit

In classical optics, there are two methods of calculating the **Resolution limit**, defined as the minimum resolvable distance (R) between two objects in order for the two objects to be distinguished from each other, (1) Abbe's limit defined by Ernst Abbe in 1873 [36] and (2) Rayleigh's criterion defined by John William Strutt, 3rd Baron Rayleigh in 1879. As shown in Equation 2.7 and Equation 2.8 respectively.

In both methods, the resolution R, of an optical imaging system (such as microscopes, cameras, telescopes) is fundamentally determined by its numerical aperture, *N.A.*, and the wavelength, λ, of the incident radiation.

$$R = \frac{\lambda}{2N.A.} \tag{2.7}$$

$$R = 1.22\frac{\lambda}{2N.A.} \tag{2.8}$$

The term numerical aperture is a dimensionless number, that characterises the range of angles that the optical system can gather/emit light determined by Equation 2.9.

$$N.A = nsin(\theta) \tag{2.9}$$

Where n is the refractive index between the optical system and the object and θ is the half angle maximum of incident beam entering/exiting the optical system. Equation 2.7 differ from the Equation 2.8 only by its coefficient.

The diffraction limit arises due to the spreading of light wave and the optical system the light passes through, the diffraction effect, that occurs at the entrance to the microscope objective. This diffraction phenomenon results in a loss of information with as discussed in Section 2.5.1. For example: A single fluoroescent protein emitting an intensity pattern (known as Airy Disk) as shown in **Figure 2.18**.

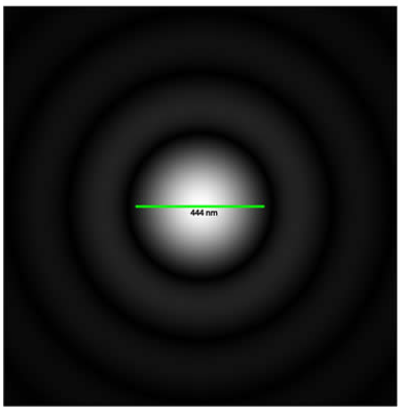

(a) Intensity profile of a single fluorophore emitting light onto a CCD camera: known as an Airy Disk

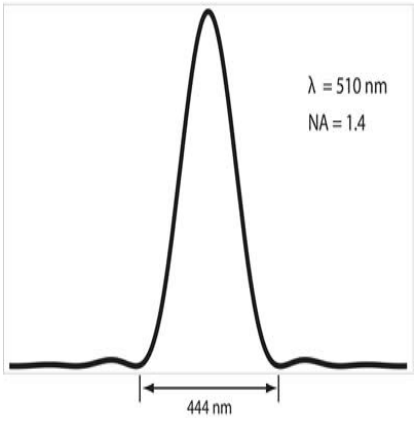

(b) Corresponding 2D intensity profile of **Figure 2.18b**

Figure 2.18 – Figure of a) Airy disk and b) corresponding 2D intensity profile.

It is clear from **Figure 2.18** above, the intensity pattern of light entering the optical system (CCD camera in this instance) is much larger than the actual size of the protein. Therefore, if multiple proteins are present within the airy profile, it would not be resolvable. This is the basis of the resolution limit: the physical distance between two point sources emitting light in relation to each other, would have to be in order to distinguish their individual light intensity pattern, or their point spread function (PSF). As shown in above resolution limits that are typically used in microscopy is the Abbe's criterion (Equation 2.4) and Rayleigh's criterion (Equation 2.5). **Figure 2.19** considers two overlapping intensity profiles of two individual specimens illustrated by the blue and red curves, and the sum of the two intensity (Airy) profiles illustrating the differences between the Rayleigh and Abbe limit. In the Rayleigh's convention, the factor of 1.22 arises from the Bessel function of first kind, since the first minima of the diffraction pattern appears at 1.22 from the central zero [37]. where the sum of the two intensity profiles shows a distinct dip. In the Abbe limit, the sum of the two intensity profiles shows a smaller dip between the maxim two maxima.

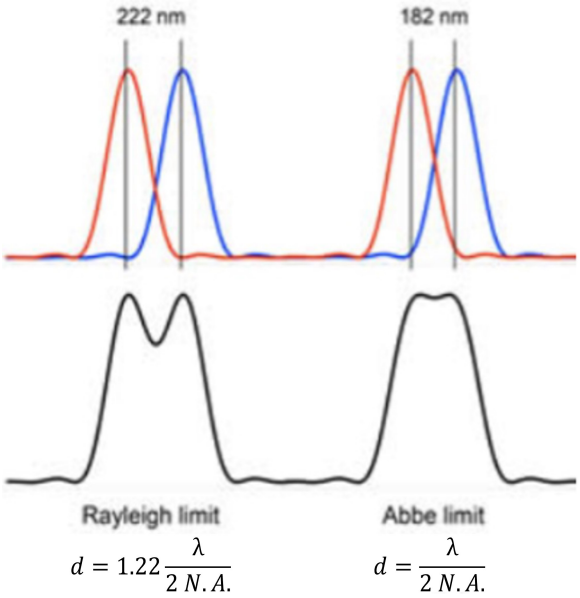

Figure 2.19 – (Upper) Intensity profile of two individual specimens, where the vertical axis corresponds to the intensity and the horizontal axis corresponds to the separation between the individual specimens. **(Lower)** The sum of the intensity profiles.

In practical applications, the difference in the results using Abbe's limit and Rayleigh's limit is small. These fundamental limits has set a barrier for the resolution of optical imaging under white light irradiation. For example, using the shortest visible wavelength (Violet - 380nm). The resolution limit using Abbe and Rayleigh is approximately 190 nm and 232 nm

respectively. This limitation not only limits resolution of image formation, it also minimum feature size during laser materials processing [38], [39].

The optical diffraction limit can be considered as an unique case of quantum mechanical phenomena using Heisenberg's uncertainty principle with respect to the position Δx and momentum Δp of a photon [38], [40].

Here p_x and x correspond to the three components momentum and position vector respectively. Consider a wave inside of a medium i, its wave vector k_i and its three components must satisfy:

$$k_i^2 = k_x^2 + k_y^2 + k_z^2 \tag{2.10}$$

Where $|k_i| = 2\ \pi/\lambda_i = \mathrm{n}_i\ |k_0|$. Where λ_i the wavelength in the medium i, n_i the refractive index of the medium, and k_0 is the wave vector in free space. In classical photonics, the light focusing effect relates only the free propagating photons. For free propagating photons, the three components are all real-values, and according to equation 2.10, this means that its 3 components k_x, k_y and k_z must be smaller them k_i. The spatial resolution the freely propagating light beam is characterized by Δx, the minimum cross-section of the freely propagating beam is thus:

$$\Delta x > \frac{1}{k_x} = \frac{\lambda_i}{2\pi} \tag{2.11}$$

From Equation 2.11, in order to obtain a small spatial resolution, the component k_x must be large. In the case where, one or more of the wave vector components for example, if k_y is complex (k_y^2 can be negative). The other components k_x and k_z can be larger than $|k_i|$ [38]. The complex component k_y corresponds to an evanescent wave, as mentioned previously, evanescent waves are the dominant waveform in the near-field, and decays within a few wavelengths from the light exiting the initial medium or aperture beyond which, the freely propagating beam becomes dominant which reverts back to Equation 2.7. Therefore, to achieve sub-diffraction limit resolutions (Super-resolution), the evanescent waves in the near-field should be utilized [41].

2.6 Optical super-resolution techniques

2.6.1 Near-field Scanning Optical Microscope

In 1928, Edward Hutchinson Synge, realising the potential of near-field evanescent waves to go beyond the optical diffraction limit, suggested using small aperture in close-proximity (nm range)of the sample to collect evanescent waves, using either a pinhole in a metal plate or a quartz cone that is coated with a metal except for at the tip [42]. Synge's idea came to fruition when the Super-resolution Aperture Scanning Microscope were demonstrated by Ash and Nicholls [43]. Advancements in nano-fabrication technologies to fabricate a sub-wavelength sized probe tips, and development of computer image processing techniques from STM (Scanning Tunneling Microscopy) and AFM (Atomic Force Microscopy), the first modern Near-field Scanning Optical Microscope (NSOM) or Scanning Near-field Optical microscope (SNOM) were demonstrated in 1991 by Betzig et al [44]. For NSOM imaging measurements, there are four possible operation modes, illustrated in **Figure 2.20** these are 1) Transmission mode imaging , 2) Reflection mode imaging , 3) Collection mode, 4) Illumination/collection mode imaging. The resolution of the NSOM technique is defined by the size of the point light source, typically achieved by coupling the light with an optical fiber the end of the fiber functioning as a NSOM tip, or AFM cantilever tips with an aperture in the center of the tip, and light is focused into this aperture. In 1984, Pohl et al demonstrated sub-wavelength resolution images consisting of 25 nm features can be recognized using Argon laser beam

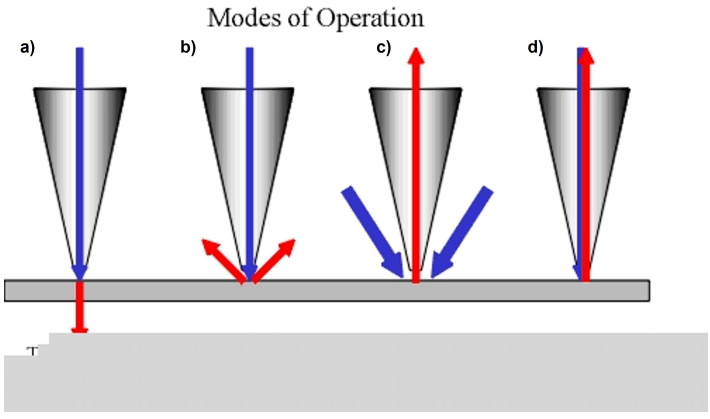

Figure 2.20 – a) Transmission mode: Light is transmitted through the sample and into a detector underneath. b) Reflection mode: Sample is illuminated through the probe aperture and the light reflected from the sample surface is collected and detected. c) Collection mode: Sample is illuminated with an external light source from the top or bottom, and the probe is used to collect the light from the sample surface. d) Illumination/collection mode: Illumination of the sample and the collection of the reflected signal is done by the probe.

(488-nm radiation) [45]. The disadvantages of super-resolution microscopy in the near-field is the "practically zero" working distance and a small depth of focus.

2.6.2 Negative refractive materials (NRMs) - Metallic Super-lenses

In 2000, Sir John Brian Pendry upon developing on the work by V.Veselago [46], suggested an method of fabricating lenses (Later known as super-lenses) whose focus is theoretically perfect [47], the artificial material (meta-material) consists of periodic structures on a scale smaller than the wavelength of incident light, such a material exhibits a negative refractive index of refraction. The unique effects of NRMs (**See Figure 2.21**) were utilized in 2005 by Fang et al to achieve sub-diffraction-limited optical imaging with a silver superlens. The experiment conducted by Fang et al is shown in **Figure 2.22** shows the comparison of FIB microscopy, AFM on photo-resist using the silver superlens, and a control experiment where the silver superlens is replaced by PMMA. NRMs are usually made of thin slabs of metals, therefore absorption of light limits its uses. Another limitation of NRM superlenses only work in the near-field by enhancing evanescent waves. The unique effects of NRMs were utilized in

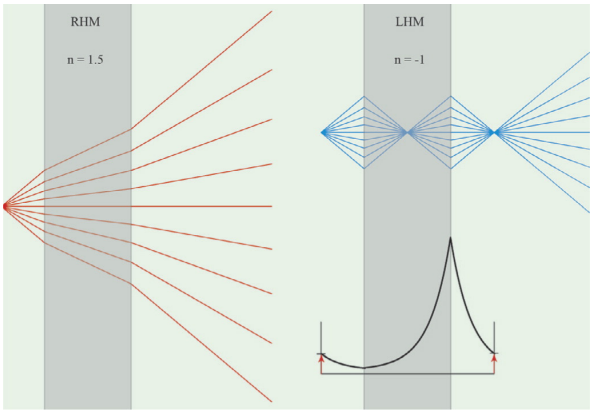

Figure 2.21 – Comparison of a normal slab of glass of n = 1.5 (left) illuminated by a point source (red), rays diverge and refract at the air/glass interface, and a slab of NRM of n = -1 (right) illuminated by a point source (blue) both governed by Snell's law and the bottom right is the evanescent component (black) of the wave from point source.

2005 by Fang et al to achieve sub-diffraction-limited optical imaging with a silver superlens. The experiment conducted by Fang et al is shown in **Figure 2.22** shows the comparison of FIB microscopy, AFM on photo-resist using the silver superlens, and a control experiment where the silver superlens is replaced by PMMA. NRMs are usually made of thin slabs of metals, therefore absorption of light limits its uses. Another limitation of NRM superlenses only work in the near-field by enhancing evanescent waves.

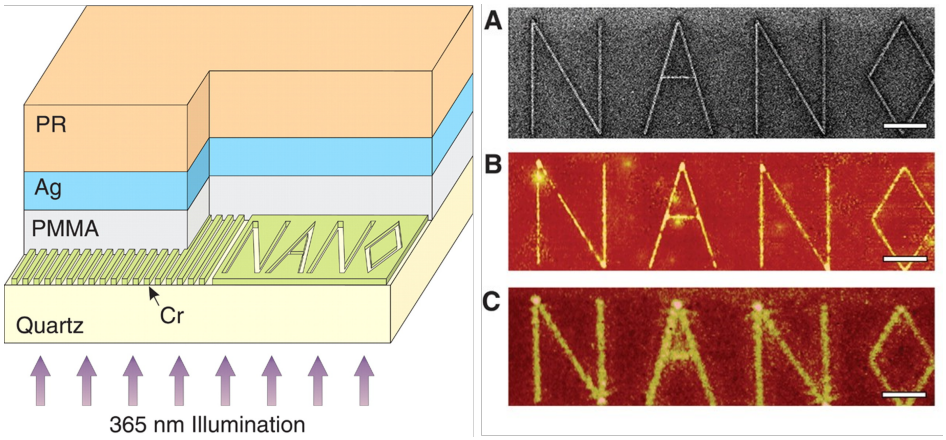

Figure 2.22 – (Left)Fang's optical superlensing experiment, the "NANO" pattern is illuminated by 365 nm through the PMMA layer and superlensing Ag layer light collected on the other side of the photo-resist (PR) is responsible for image formation. (Right) Silver supenlens image of embedded "NANO" pattern of line width 40 nm- A) Focus ion beam imaging, B) Atomic Force Microscopy (AFM) on photo-resist using silver superlens C) Control experiment where the silver superlens layer is replaced by 35 nm thick PMMA. Scale bar is 2 μm

2.6.3 Photonic Nanojet

In 2000, Lu et al. demonstrated a near-field optical enhancement effect using 0.5μm silica spheres to pattern on (100) silicon substrate [48]. Since 2004, the term 'photonic nanojet (PNJ)' was proposed by Chen et al. [49] to describe the near-field optical enhancement phenomena has become the widely known term within the optics community. Unlike NRM above, which uses metals to enhance evanescent waves. The microspheres can use dielectric materials such as silica and polystyrene, thus less light absorption. PNJ is a narrow high-intensity EM beam that propagates into the background medium from the shadow side surface of a plane-wave illuminated lossless dielectric micro-cylinder or micro-sphere of diameter greater than the wavelength of incident light. PNJ enables the possibility of focusing light beyond the diffraction limit and this can be utilized for microscopy as well as laser micro/nano patterning applications, to operate in the far-field. **Figure 2.23** shows the visualisation of PNJ irradiated with 400 nm laser, with different sizes of microspheres.

2.6.4 Key properties of PNJ

PNJ are described by four distinct characteristics as discussed in Heifetz [50]:

1. It is non-evanescent, maintaining sub-wavelength FWHM transverse beam width more than 2λ beyond the micro-sphere/ micro-cylinder
2. Minimum FWHM beam-width can be smaller than the classical diffraction limit.
3. Non resonant phenomenon that can appear for a wide range of dielectric micro-cylinder or micro-sphere diameters (from 2λ to 40λ) provided that the refractive index ratio between the dielectric and background medium is approximately 2:1.
4. Its intensity can significantly exceed the incident wave
5. Introducing a nano-particle of diameter d_v inside of the PNJ stream has an effect that can enhance the back-scattered power.

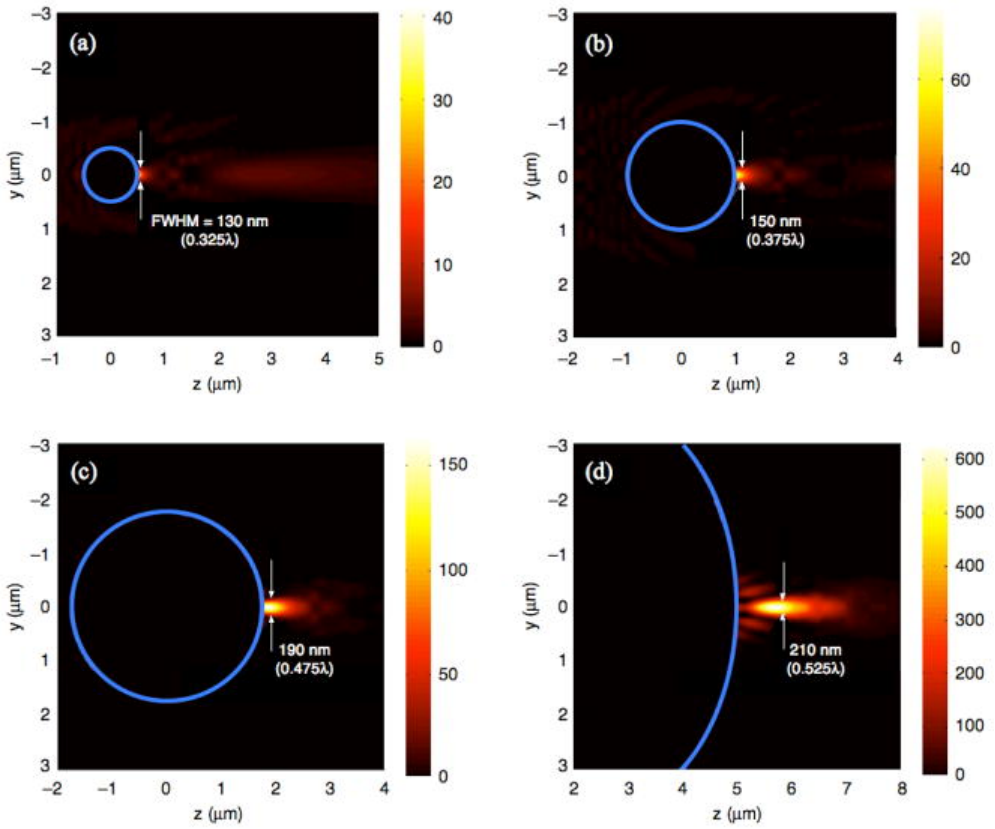

Figure 2.23 – Simulation of PNJ generation from microsphere of refractive index, n = 1.59 in vaccuum a) 1 μm b) 2 μm c) 3.5μm and d) 8 μm. Taken from Chen [7]

2.7 Micro-sphere marking techniques

2.7.1 PCM lens

In 2020, Yan et al reported a new high-performance all-dielectric lens, formed by combining a conventional plano-convex lens with a high-index microsphere (BTG, n = 1.9 - 2.1) lens (PCM), for far-field super-resolution applications [51]. The PCM lens been reported to have a theoretical resolution of $\sim \lambda/2.5$ in air with a working distance of $\sim 2\mu$m away from the lens. The unusual focusing properties of the PCM lens (**photonic nanojet**) were discussed, and the reason for the practical resolution being better than the experimental resolution was due to the nonlinear absorption response of the processed material. The PCM lens was combined with the 100 fs laser, the practical patterning resolution reached $\sim \lambda/3.5$. Photonic nanojet phenomena enabled the laser to be focused to the nano-scale. Arbitrary patterns were demonstrated using this technique as shown in **Figure 2.24**.

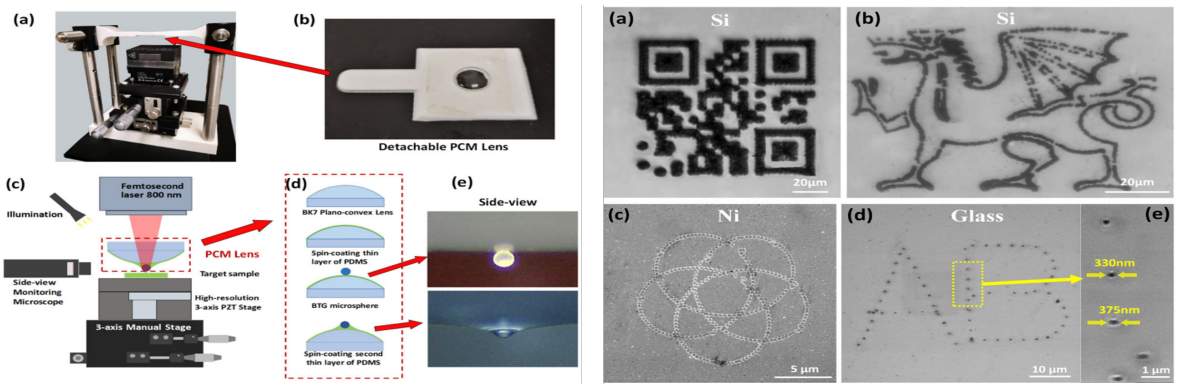

Figure 2.24 – (Left) (a) PCM lens setup, (b) Detachable PCM lens module, (c) Schematic diagram of the experiment setup, (d) Procedure of fabricating PCM lens. (Right) (a) QR code marked on Si wafer, (b) Welsh dragon on Si wafer, (c) Guilloche pattern on nickel substrate, (d) AB letter on glass substrate, (e) Magnified image of the highlighted area

2.7.2 Micro-sphere array marking

Many studies have combined the micro-lens array (MLA) assisted technique with laser processing techniques (different wavelengths, and/or different pulse duration lasers) for nano-hole fabrication [52], [53], metallic surface functionalization [54], and micro/nanopatterning. In 2010, Pena et al published the findings of direct writing of micro/nano-scale Nd:YVO_4 laser [55]. The use of a 5 μm SiO_2 particle lens array enables the combination of conventional laser marking with a particle assisted laser fabrication technique to create micro-patterns (See **Figure 2.25 a - c**) consisting of nano-scale ($\sim$564 nm) holes.

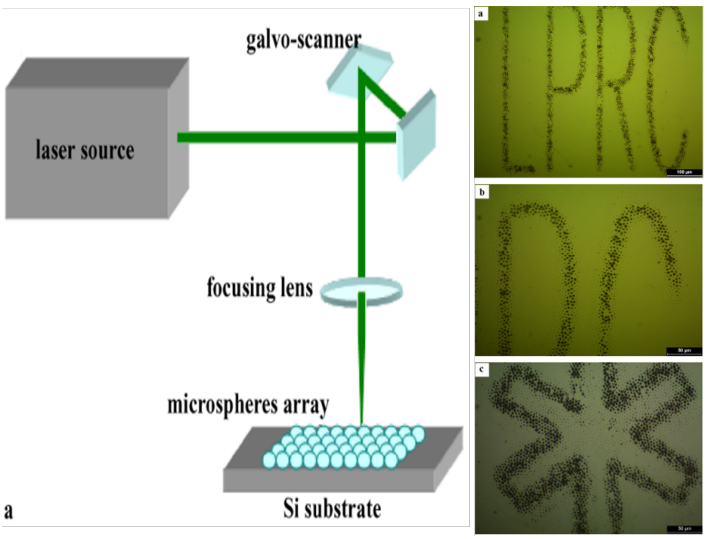

Figure 2.25 – Schematic of the experimental setup in [55]

This technique allows enables for rapid fabrication of micro-nano patterns as each laser-illuminated microsphere on the substrate produces individual photonic nanojet for nano-hole laser marking. However, the techniques of producing a high-quality mono-layers rapidly and reliably require further investigations.

2.8 Self-assembly mono-layer

In order to enable microsphere array laser marking on any substrate, understanding the underlying mechanisms to fabricating a HCP (Hexagonal close packed) particle-lens array is essential and literature review of the Coffee Ring effect (CRE), and investigation of the experimental approaches such as drop-casting, spin-coating, Langumir-Blodgett method (LB) and Langumir-Schaefer (LS) were conducted to determine which technique to use for the Dot Code marking experiment.

2.8.1 Drop-casting

Drop casting is a simple, rapid technique that is widely used to modifying substrate surfaces is composed of particles such as nanotubes or nanoparticles. The technique allows for the formation of mono-layers by dropping colloidal solution onto a flat substrate, followed by the evaporation of the droplet as shown in **Figure 2.26**. However, this technique requires consideration of the influence of coffee ring effect, which is induced by capillary flow within the droplet which inhibits the formation of large-area mono-layers.

Coffee ring effect

The coffee ring effect (CRE) is an phenomenon observed when, the evaporation of droplets containing suspended particles forms a ring-like pattern upon drying. This effect originates at

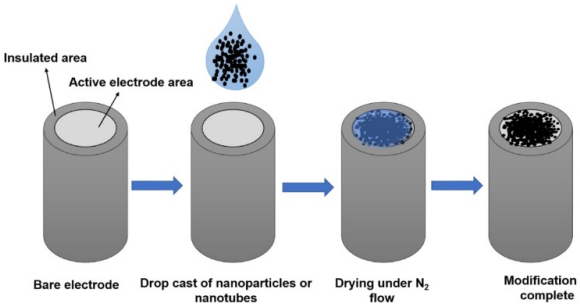

Figure 2.26 – Illustration of drop casting technique onto an electrode

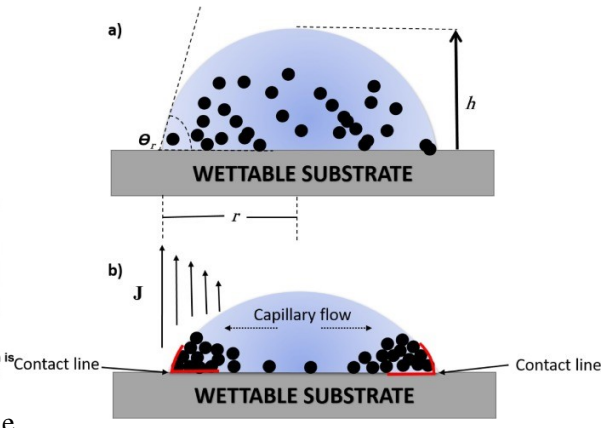

Figure 2.27 – Coffee ring effect: the capillary flow within the droplet causes aggregation of the particles on the outer edges of the droplet.

the edge of the droplet confining the droplet from further spreading of the droplet. Evaporation at the edge of the droplet is faster than in the centre of the droplet, since at the edge is more exposed to its surroundings [56]. The greater solvent loss at the edges of the droplet is compensated by the flow of solvents from the centre outward, known as the capillary flow. Illustration of the effect is shown in **Figure 2.27**. where θ_r is the contact angle, h is the height of the droplet, r is the radius of the droplet, and **J** is the evaporation flux. There are several techniques to ameliorate the effect of CRE, such as the use of super-hydrophobic surface [57], [58], acoustic waves [59], [60] or by inducing a Maragoni flow to counterbalance the capillary flow.

2.8.2 Spin-coating

Spin coating is a type of thin-film deposition technique in which utilises centrifugal force to spread a solution uniformly on a flat substrate. For spin coating, the apparatus used is called a spin coater, the equation of the thickness of film, h_f is given in Equation 2.12.

$$h_f \propto \frac{1}{\sqrt{\omega}} \tag{2.12}$$

In Ogi [61], mono-layers of 550 nm and 300 nm silica microspheres were rapidly deposited onto a sapphire substrate, with preparation time lasting only 25s. An illustration of the phenomena that occurs during spin coating is shown in **Figure 2.28**. In Khanna [62], fabrication of long-range ordered close-packed mono-layers of 200 nm silica spheres deposited onto a n-type silicon substrate were demonstrated, using a triple-step spin process, Step 1) 200 RPM for 10 seconds, Step 2) 500 RPM for 30 seconds, Step 3) 1500 RPM for 60 seconds.

Figure 2.29 shows the procedures and its results of the experiment. The disadvantage of this technique is the requirement of the initial droplet to be directly in the centre of the substrate also, the spin parameters requires rigorous testing dependent on the viscosity of the solution to achieve desirable results.

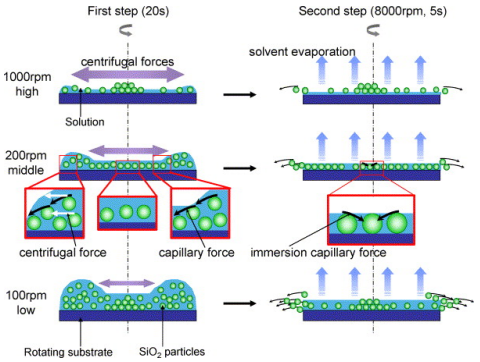

Figure 2.28 – Illustration of possible phenomena occurred during spin coating of SiO_2 particles at each spin speed as a result of centrifugal forces and solvent evaporation. Taken from [61].

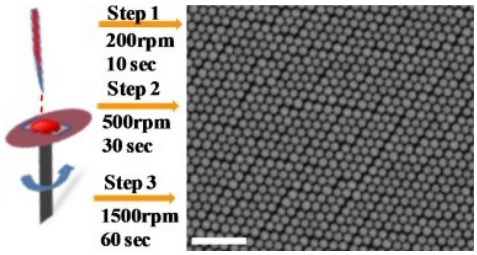

Figure 2.29 – Spin coating experiment conducted in [62] to achieve a long-ranged close-packed monolayer of silica nanospheres.

2.8.3 Langmuir-Blodgett method

In 1917, upon developing on the work by A.Pockels [63]. I.Langumir and K.Blodgett demonstrated that that single water-air interface monolayers could be transferred to solid substrates using a device known as the Langumir-Blodgett trough as shown in **Figure 2.30**. Langumir-Blodgett method is a technique to forming mono-layer films onto an arbitrary substrate that is widely used in the production of electronic equipment such as semiconductor [64], [65], biosensors [66], [67], and recently, algal biophotovoltaic fuel cells [68]. The

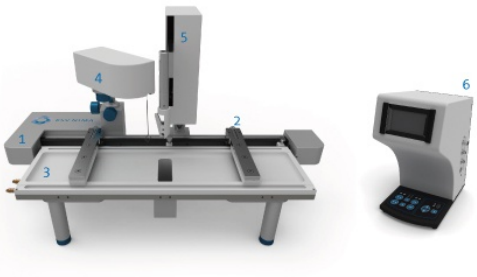

Figure 2.30 – Langmuir-Blodgett trough 1) Frame 2) Barriers 3) Trough top 4) Surface pressure sensor 5) Dipping mechanism 6) Interface unit

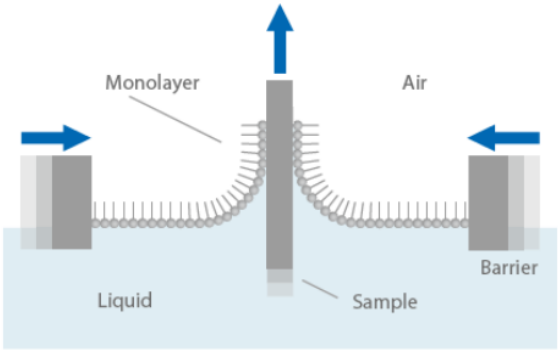

Figure 2.31 – Illustration of the LB method

Langmuir-Blodgett troughs are operated by dropping a colloidal solution of nano-particles onto the surface of a liquid, then the nano-particles spreads evenly across the surface of

the liquid to form a self-assembled mono-layer (SAM) the barrier then closes (compression speed dependent on the nano-particles), compressing the mono-layer onto the vertical sample substrate surface, the sample is then slowly pulled upwards allowing for the mono-layer to form vertically onto the sample surface.

2.8.4 Langmuir-Schaefer method

Langmuir-Schaefer (LS) method is similar to the Langmuir-Blodgett method in that the Langmuir-Blodgett trough is also used to compress the nano-particles into a mono-layers then transferred onto a sample surface. LS method places the sample surface parallel to the liquid then the transfer of nano-particles from the liquid surface to the sample is complete [69]. LS method has been employed in similar applications to LB method. such as sensors [70] deposition of quantum dots for various applications [71].

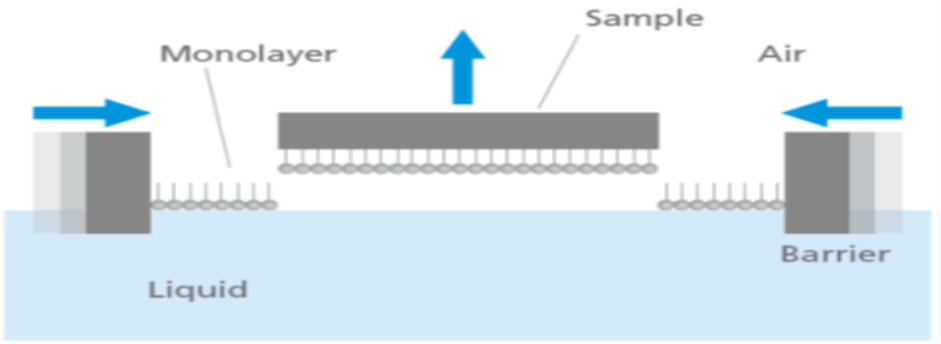

Figure 2.32 – Illustration of LS method, Barrier closes to compress the nano-particles into a mono-layer, the mono-layer are transferred onto the sample parallel to the liquid surface.

Chapter 3

RESEARCH METHODOLOGY

Section 3.1 - 3.3 describes the laser systems (Femtosecond laser, UV nanosecond laser), sample characterization setups (laser confocal microscopy, AFM and SEM) and the readout scanner application used in this project.

Section 3.4 describes the experiment preparation procedures for mono-layer fabrication, highlighting the factors that may cause aggregation and methods of limiting the aggregation.

Section 3.5 describes the three different experiments (drop-casting, spin-coating, modified LS) of fabricating mono-layers

Section 3.6 describes the femtosecond and UV laser marking experiments

Section 3.7 describes the theoretical work, simulation software and the proposition of a blob detection method to aid a successful readout of the fabricated Dot code.

3.1 Experiment laser systems

3.1.1 Femtosecond laser

The wavelength of the laser is 800 nm and pulse duration is below 100 fs. The details are shown in the table below. The laser system is equipped with a SDG-2 (Synchronisation and Delay Generator) box to trigger single pulses. The Dot Codes are laser-marked by programming a motorised stage within the femtosecond laser setup shown in **Figure 3.1**.

Maximum output power	1 W
Wavelength, λ	800 nm
Pulse duration, t (fs)	<100 fs
Repetition Rate, f	5kHz
Beam size, r	$\sim$30 μm

Figure 3.1 – Photograph of the femtosecond laser used in the experiment

3.1.2 UV nanosecond laser

The UV laser setup was used to conduct the nano-scale hole marking experiment, the UV laser setup consists of the manual Z-stage to fine-tune the Z-position of the substrate (Resolution = 0.5 μm). The wavelength of the UV Laser is 355 nm, repetition rate was set to 50 kHz during experimentation, the output power as a function of the Q-pulse duration was measured prior to experimentation and displayed in **Figure 3.2a)** and the photograph of the UV Laser setup is shown **Figure 3.2b)** beam size is approximately 50 μm. The scanner has a field size 200 mm x 200mm and a focal length of 290 mm.

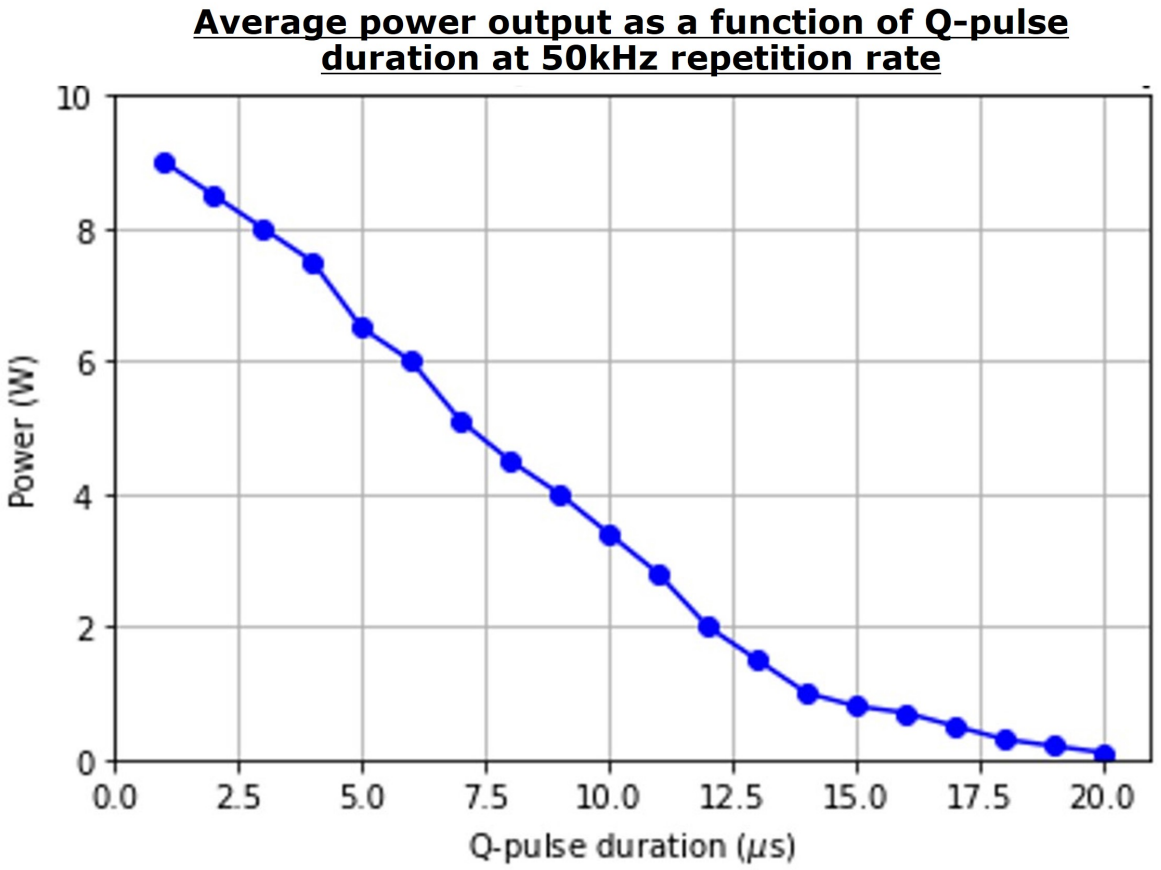

(a) Average power output as a function of Q-pulse duration at 50kHz repetition rate

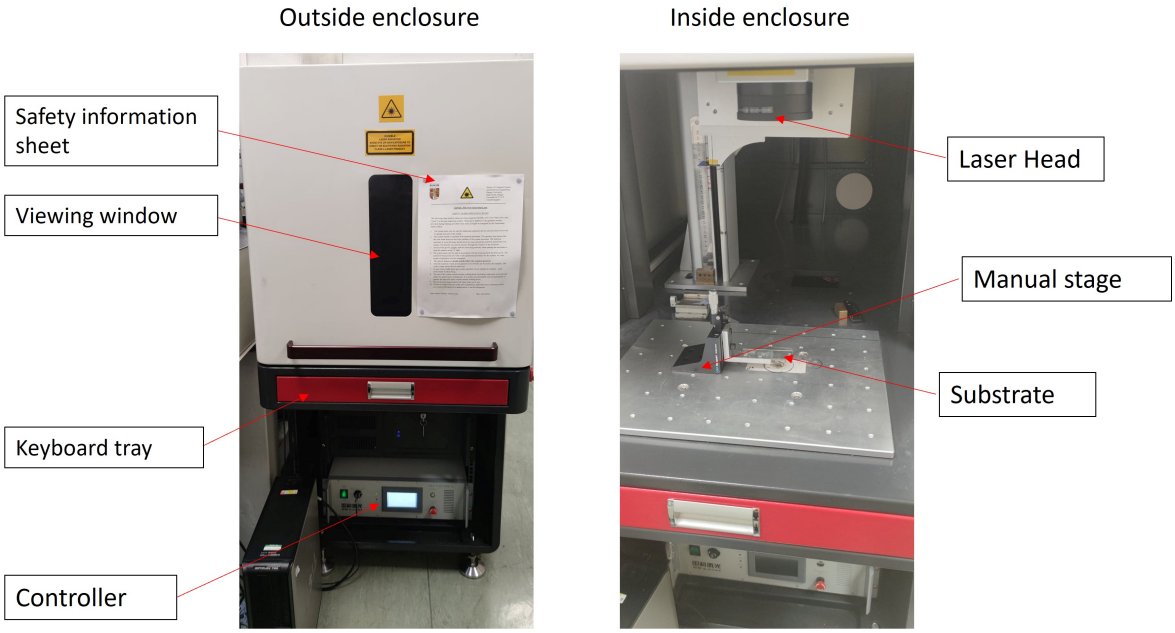

(b) Photograph of UV laser setup

Figure 3.2 – (a) Graph of power output as a function of Q-pulse duration at 50kHz repetition and photograph of UV laser setup used in the experiment.

Q (µs)	Sample ID	Power (W)	Pulse (J)	Fluence (J/cm²)
12.1	1	1.95	0.000039	1.98625369
12.2	2	1.9	0.000038	1.935324108
12.3	3	1.85	0.000037	1.884394526
12.4	4	1.8	0.000036	1.833464944
12.5	5	1.75	0.000035	1.782535363
12.6	6	1.7	0.000034	1.731605781
12.7	7	1.65	0.000033	1.680676199
12.8	8	1.6	0.000032	1.629746617
12.9	9	1.55	0.000031	1.578817035
13	10	1.5	0.00003	1.527887454
13.1	11	1.45	0.000029	1.476957872
13.2	12	1.4	0.000028	1.42602829
13.3	13	1.35	0.000027	1.375098708
13.4	14	1.3	0.000026	1.324169127
13.5	15	1.25	0.000025	1.273239545
13.7	16	1.15	0.000023	1.171380381
13.9	17	1.05	0.000021	1.069521218
14.1	18	0.98	0.0000196	0.998219803
14.3	19	0.94	0.0000188	0.957476138
14.5	20	0.9	0.000018	0.916732472
14.7	21	0.86	0.0000172	0.875988807
14.9	22	0.82	0.0000164	0.835245141
15.1	23	0.79	0.0000158	0.804687392
15.3	24	0.77	0.0000154	0.78431556
15.5	25	0.75	0.000015	0.763943727
15.7	26	0.73	0.0000146	0.743571894
15.9	27	0.71	0.0000142	0.723200061
16.1	28	0.68	0.0000136	0.692642312
16.3	29	0.64	0.0000128	0.651898647
16.5	30	0.6	0.000012	0.611154981

Figure 3.3 – List of UV laser parameters used in this project, pulse energy and laser fluences were calculated based on repetition rate of 50kH and spot size of 50 μm

3.2 Sample characterization setup

3.2.1 Confocal microscopy

Olympus LEXT™ OLS5100 3D Laser Confocal Microscope (**Figure 3.4**)was used to characterise the quality of the silica microspheres monolayer mask and the laser marked 2D micro DotCodes. The microscope is equipped with Olympus MPlanFL N semi-apochromat objective lenses ranging from 5x to 100x magnification. the objective lenses specifications is shown in **Table 3.1**. The images obtained are transferred into the PC and measured within the built-in data acquisition application. Samples can be moved via a motorised stage, controlled with a stick controller or directly within the data acquisition application.

Figure 3.4 – Olympus LEXT™ OLS5000 3D Laser Scanning Microscope

Magnification	Numerical Aperture	Working Distance (mm)
5x	0.15	20.00
10x	0.30	10.40
20x	0.60	1.00
50x	0.95	0.35
100x	0.95	0.35

Table 3.1 – Specifications of optical lenses

3.2.2 AFM - Atomic Force Microscopy

Veeco Dimension 3100 AFM machine with a Dimension V(5) controller (**Figure 3.5**) was utilised to measure the width and depth of the nanoholes marked, the resolution of the AFM machine is ultimately determined by the properties of the tip, including mechanical sharpness and the resolution of the vertical scanner movement, given the age of the tip, the resolution may have been slightly higher than the reported 10-20nm in the manual.

(a) Photograph of the AFM machine exterior

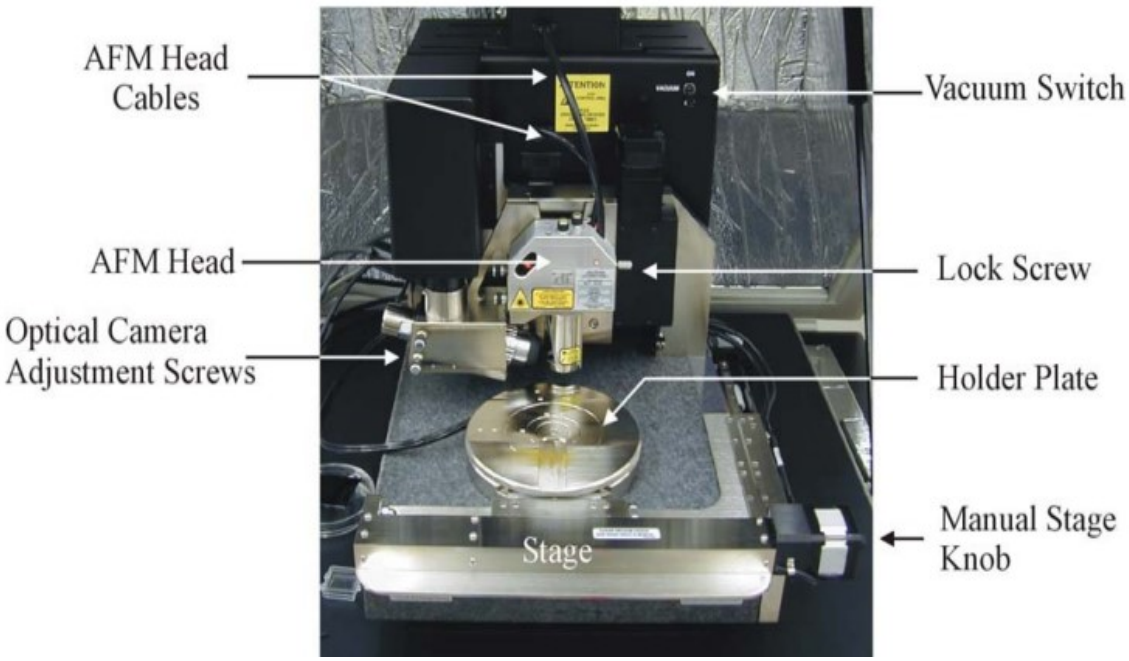

(b) Photograph of the AFM machine interior

Figure 3.5 – Photograph of the Veeco Dimension 3100 AFM machine.

3.2.3 SEM - Scanning Electron Microscopy

Hitachi Tabletop Microscopes TM4000II (**Figure 3.6**) was used to inspect the mono-layer prior to marking with the laser system. The operating principle of the SEM, which uses accelerated electrons focused onto the sample, depending on the morphology of the sample, number of secondary electrons emitted from the sample detected will be detected to produce an image. The TM4000II microscope is capable of achieving magnifications of 10 × - 100,000 × (Photographic magnification) and 25× - 250,000× (monitor display magnification).

Figure 3.6 – Hitachi Tabletop Microscopes TM4000II / TM4000Plus II used.

3.3 Pattern recognition

The pattern recognition in this project is done by using a downloadable mobile phone barcode scanner application, **Barcode scanner** made by Cognex corporation, **Figure 3.7** and **3.8** shows pattern recognition of the Dot Code. The recognition application capabilities of this application extend beyond Dot Code and can recognise other types of barcode such as QR codes, Aztec barcode etc.

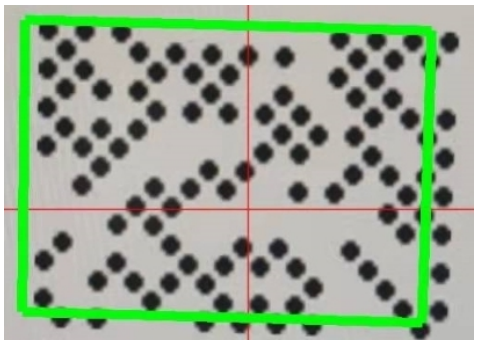

Figure 3.7 – Scanning the Dot Code.

Figure 3.8 – Decoded Dot Code - Bangor 2022.

3.4 Experiment preparation

3.4.1 Substrate preparation

1. Cut the substrates to a suitable size for the experiment using the diamond tip glass cutter.
2. Wipe the substrate with 99% isopropyl alcohol
3. Prepare a container of acetone and place into ultrasonic bath.
4. Sonicate the substrate in acetone for 20 minutes.
5. Prepare a container of ethanol and place into ultrasonic bath.
6. Sonicate the substrate in ethanol for 20 minutes.
7. Submerge the substrate in ethanol in a sealed container for storage.
8. Dry with N_2 gas and use in experiment immediately.

3.4.2 Micro-sphere colloidal solution preparation

The 1.18 um microspheres used in this experiment were manufactured by Cospheric.
Dry mono-disperse Silica Microspheres 2.0g/cc d50=1.18um, CV=2.5%, <1% Doubles - 1g.
This section highlights the mechanisms considered when attempting to fabricate a high-quality mono-layer for colloidal lithography for the Dot Codes. Dry dielectric silica microspheres are prone to electrostatic effects that causes aggregation (clustering of microspheres), preventing the possibility to making a high-quality microsphere mono-layer, unless the microspheres are fully dispersed into a colloidal solution. Using the knowledge of the factors that contribute to the aggregation of silica microspheres above, the following procedures were used to disperse the silica microspheres as highlighted in [72]:

1. Prepare solvents in an empty vial (e.g ethanol, methanol, acetone etc.)
2. Prepare 1-2% wt of the silica powder (microspheres) (1 g of solvent = 0.02 g of microsphere).
3. Grind all visible clumps of silica powder to a fine powder with pestle and mortar.
4. Add the fine silica powder into the solvent vial.
5. Rigorously vortex the silica suspension vial with a magnetic stirrer, at 1500 RPM for 20 minutes.
6. Sonicate the suspension vial into ultrasonic bath for 10 minutes. *(Probe sonication is not advised for dispersing powders)*

7. Confirm that the microspheres are fully dispersed under confocal microscope with single droplet of suspension.
8. Repeat from step 5 if the suspension is not fully dispersed.

3.4.3 Preventing aggregation

It is important to understand the factors that cause the aggregation of the microsphere after fully dispersing. As highlighted in [73], size of microsphere, the temperature, concentration of microspheres contribute to the aggregation of microspheres.

Particle size

The probability of aggregation increases as the size of the microspheres decreases as random (Brownian) motion of the smaller ($< 1\mu$m) dispersed microspheres causes the hydrophobic interactions (the tendency for non-polar molecules to aggregate in solution) to more likely occur. For sub-micron microspheres, maintaining a mono-dispersed suspension may not be possible without the use of additional surfactant (To alter the hydrophobicity and/or surface charge of the microsphere), or lowering the microsphere concentration of the suspension.

Temperature

Temperature is interlinked with the kinetics of the microspheres in suspension, an increase in temperature causes an increase in the kinetics of the microspheres in suspension. Therefore, collisions between microspheres is more probable, and subsequently, the probability of hydrophobic interaction causing aggregation is more probable.

Surface Charge

Colloidal particles are mostly charged in an aqueous solution because of the protonation or deprotonation of ionizable groups on the surface [74]. The colloidal stability (tendency to remain mono-dispersed), depend on the positive or negative surface charge of the microspheres [75]. The electrostatic repulsion between the microspheres in the colloidal suspension play a major role in preventing aggregation.

Concentration

The higher the concentration of the microspheres in suspension, the higher the probability of collision and the hydrophobic interactions which causes aggregation. Typically a concentration between 1-10% is used for mono-layer deposition applications.

Silica Micro-spheres

Cospheric 1.18 μm silica microspheres used in this experiment are inherently hydrophillic, this property lowers the probability of the hydrophobic interaction. According to the manufacturer,

the aggregation problem with silica microspheres is more commonly associated with charge interactions between microspheres, or incomplete separation during microsphere formation. For this reason, the preparation procedures follow [76] where more physically aggressive grinding approach were used with a pestle and mortar.

3.5 Experimental methods - Mono-layer fabrication

3.5.1 Drop-casting approach

The drop casting approach, 1% and 2% colloidal suspension of 1.18 μm dispersed in deionised water, ethanol, methanol and an ethanol/methanol mixture were used, colloidal droplets using a syringe and needle were dropped onto the glass/ Al thin film substrates are placed onto goniometer stage at an angle of ranging from 1°to 10°. The setup is then placed inside of a refrigerator for 24 hours to allow for the droplet to evaporate slowly, to attempt to allow for sufficient time for self-assembly into a HCP mono-layer. **Figure 3.9** shows the a schematic diagram and a photograph of the drop casting setup.

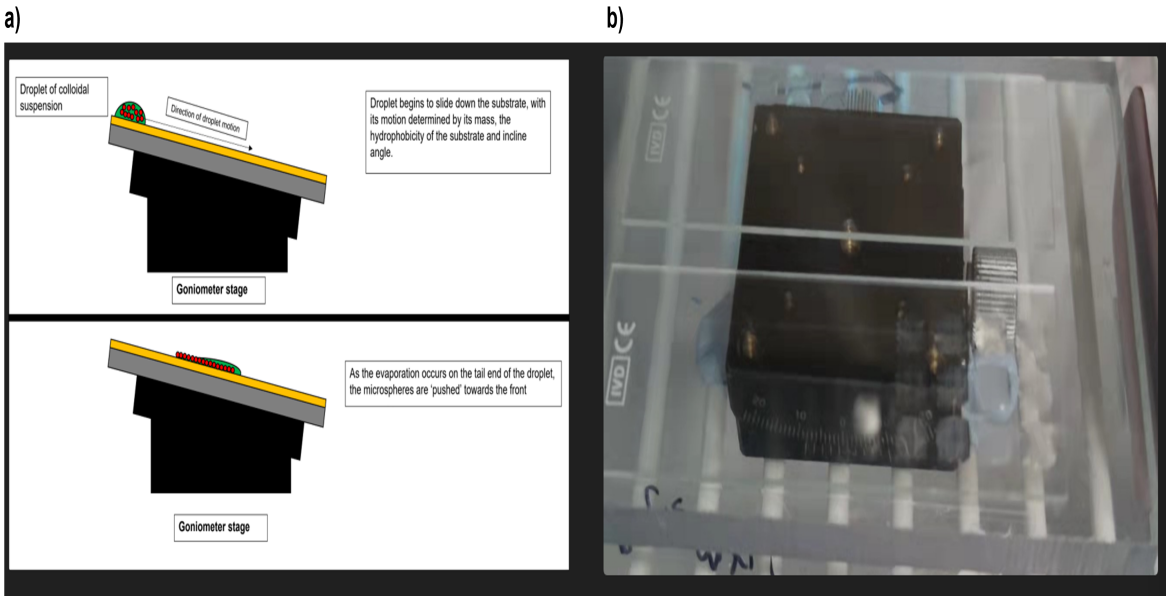

Figure 3.9 – a) Schematic drawing of the drop casting setup b) Photograph of the drop-casting setup

3.5.2 Spin-coating approach

In order to fabricate a large area mono-layer of silica particles spin coating, this approach follows the work Ogi et al. 2007 [61] and Khanna et al. 2018 [62] where the effects of 1) surface treatment, 3) spin speed and 4) concentration of suspension were investigated with silica nanospheres of size, 300 nm, 550 nm (Ogi) and 200 nm (Khanna).

In this experiment, the spin coater (**See Figure 3.10**) were pre-set to spin in three stages at 200, 500 and 1500 RPM. With the glass slide being prepared from using the substrate preparation section.

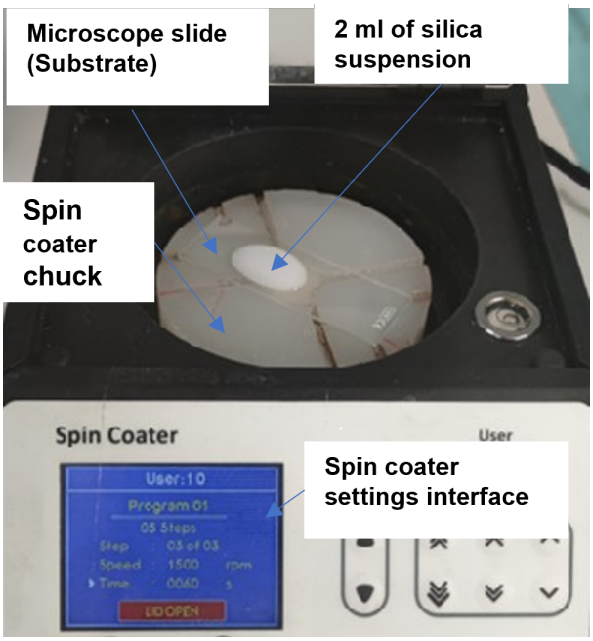

Figure 3.10 – Photograph of the spin-coater setup used in the experiment

3.5.3 Modified Langmuir-Schaefer method

The method of depositing a HCP mono-layer of silica micro-spheres onto an arbitrary substrate to enable simultaneous marking is adopted from J.Hruby et al. [77] and V.Lotito et al. [78]. In both studies, the deposition of an arbitrary spherical particles were achieved by submerging the substrate in water, and the particles in suspensions are deposited onto the water/air interface for self-assembling inside of an area-confining barrier, then as the water released from the apparatus, the mono-layer formed on the water/air interface is lowered onto the substrate below. Although the reason for using water is not specified, it is well-known that besides, mercury, water has the highest surface tension of all liquids [79]. The idea of this approach is to allow the colloidal microspheres to self-assemble on the surface of water, and then lowered onto a substrate below as illustrated in **Figure 3.11**. Schematics of both apparatus is shown in **Figure 3.12** and **3.13** below.

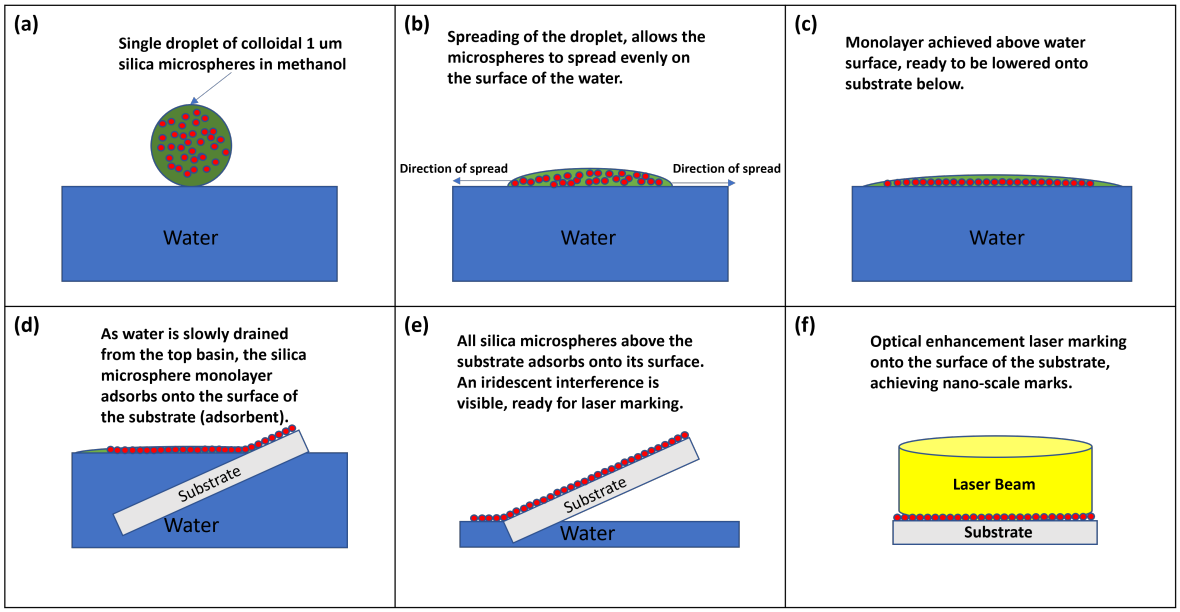

Figure 3.11 – Illustration of the preparation of self-assembled silica mono-layer for simultaneous laser marking.

3.5.4 Hruby apparatus

In Hrubý's experiment, the deposition of the Qubits onto water surface then compressed into a close packed mono-layer were achieved by using a Langumir-Blodgett trough to compress the spheres into a close packed structure, then lowered onto a substrate below.

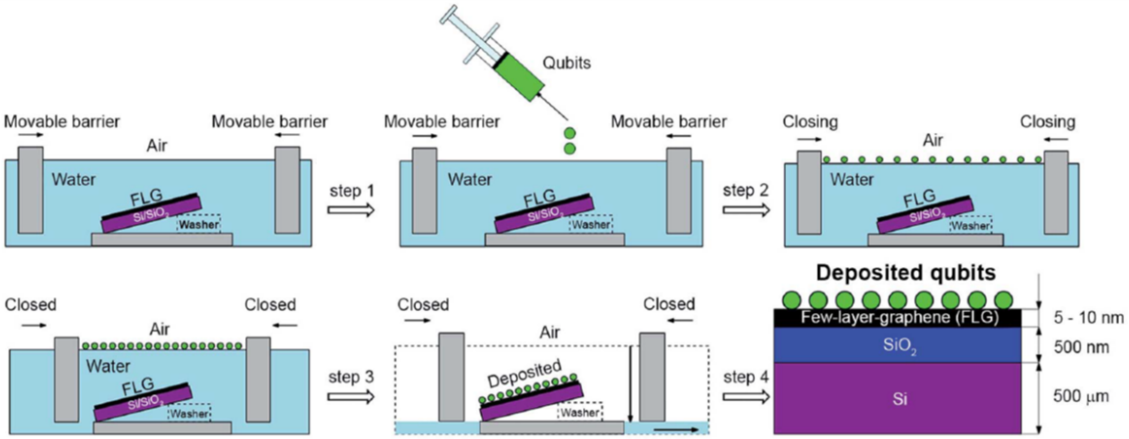

Figure 3.12 – Scheme of the modified Langumir-Schaefer method used in [77]. Initially, the FLG covered Si/SiO_2 substrate is submerged in deionised water. Step 1: the solution of Qubits (a suspension of copper(II)dibenzoylmethane $[Cu(dbm)_2]$) is added onto the water/air interface. Step 2: Qubits particles spreads upon the water/air interface and the movable barrier closes pushing the particles to closed packed structure. Step 3: Water is released from the apparatus, lowering the close packed onto substrate below. Step 4: The final close packed mono-layer composed of $[Cu(dbm)_2]$ deposited onto the substrate

Lotito apparatus

In Lotito's apparatus design, the self-assembly of (200nm, 300nm and 1000nm) PS colloidal micro-spheres were achieved air/water interface and confined within a nitrile butadiene rubber ring, as water is discharged from the container via a controllable tap, the self-assembled mono-layer on the water/air interface is lowered and transferred onto the substrate below as water is drained from the container.

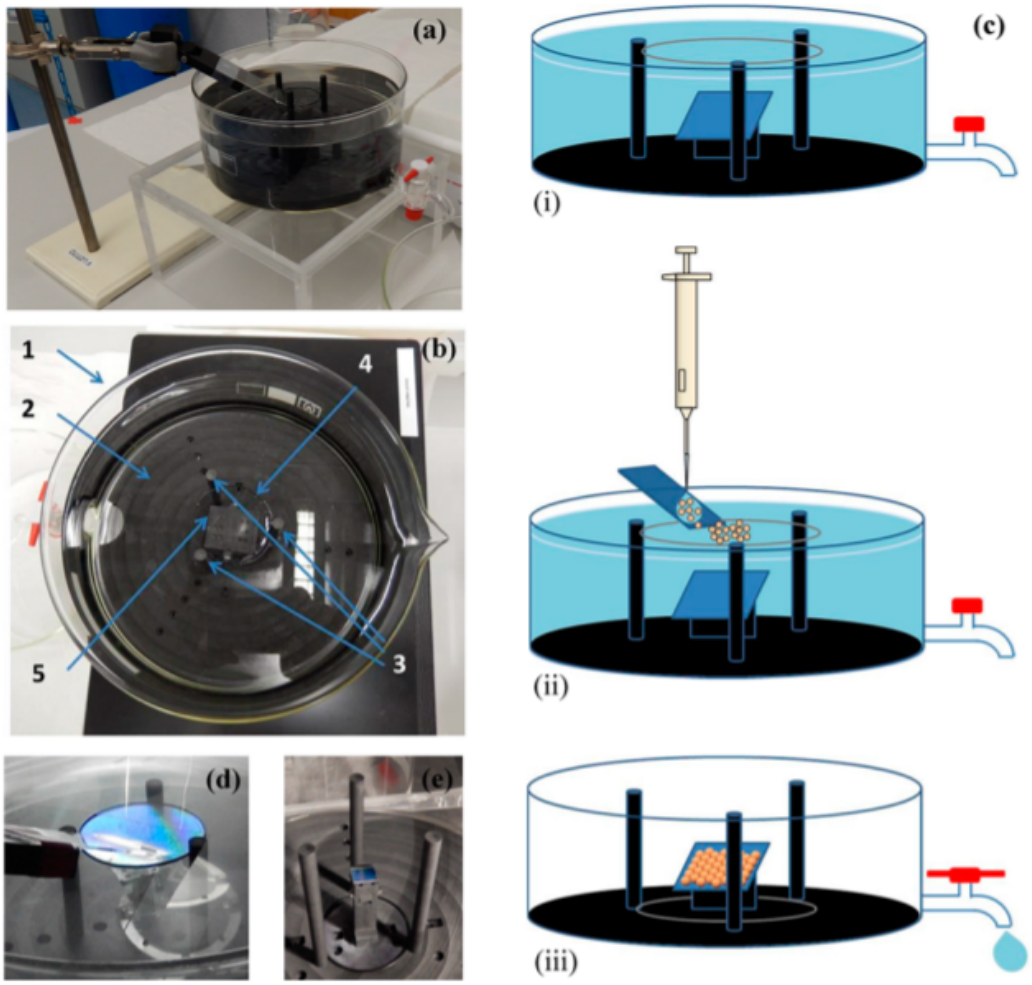

Figure 3.13 – (a) Photograph of setup; (b) Details of the setup (1) glass container with built-in tap, (2) Carbon-filled PTFE Circular plate, (3) Carbon-filled PTFE Cylindrical rods (4) NBR O-ring (5) Carbon-filled PTFE sample holder; (c) (i) Sketch of apparatus, (ii) Deposition of PS microsphere onto water surface, (iii) Water discharged from the tap, self-assembled mono-layer deposited onto substrate. Taken from [78] 2016.

Customised apparatus

The custom design of the apparatus used in the project (See **Figure 3.14**), were made with low-cost components and it consists of a top cup made of polystyrene (PS) with four bamboo sticks glued to the bottom of the PS cup, which functions as O-ring confinement rods. The top cup is placed onto platform made from a plastic sheet and four wooden sticks in a larger cup underneath for water collection during discharge. Initially covered with blu-tack, an orifice is created by puncturing the bottom of the PS cup with a needle for water discharge into a larger PS cup underneath, and the orifice is resealed with blue-tack after use. Since the

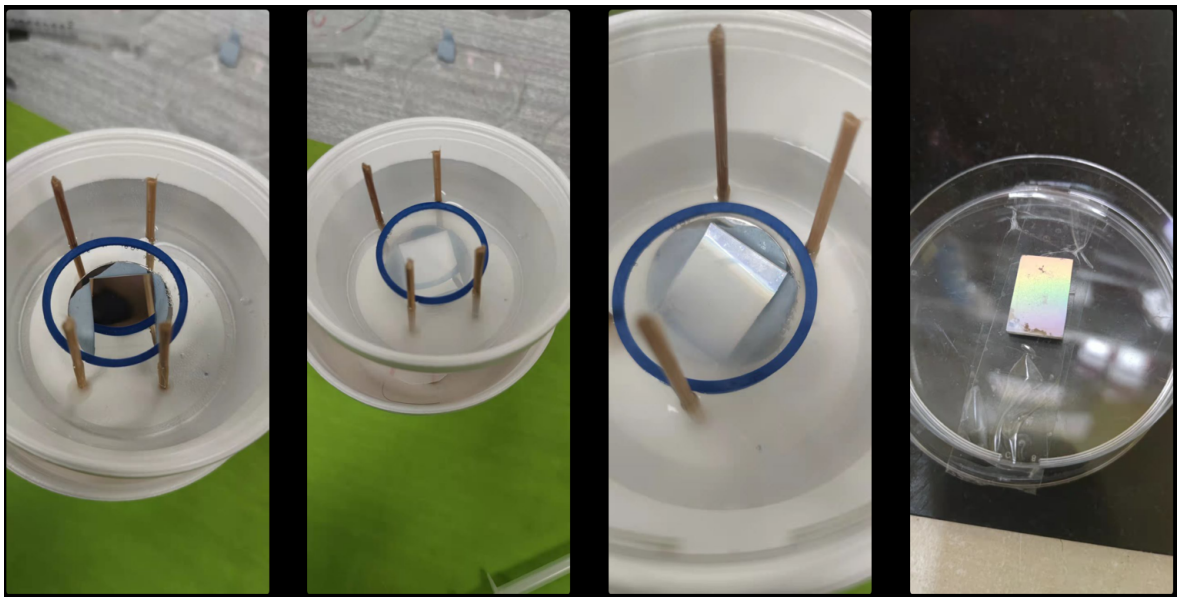

Figure 3.14 – Photograph of the preparation process onto Aluminium thin film: (Left) Apparatus filled with water; (Center Left) Colloidal suspension added inside the nitrile ring; (Center Right) Adsorption of microspheres onto substrate d) (Right) Result of Mono-layer deposited onto substrate displaying opalescence interference effect.

density of silica (2.20 g/cm^3) being higher than the density of water (1 g/cm^3), the 1 μm silica micro-spheres were suspended in methanol, this forms a methanol layer above the water/air interface (Methanol density = 0.792 g/cm^3). The low interfacial tension of methanol [80], [81] causes spreading of the colloidal suspension above the water/air interface, as the contact angle of the methanol on water decreases, the interfacial forces associated with the spreading assists in compressing the microspheres into a hexagonal closed packed (HCP) mono-layer. Another useful property of using methanol for the innovated apparatus is the evaporation rate (0.149 picogram/minute) [82], its slow evaporation rate allows sufficient time for the microspheres to spread evenly on the water surface.

3.6 Experimental methods - Laser marking

3.6.1 Direct laser marking initial experiment

Femtosecond laser pulses were used to directly marking DotCodes onto a soda-lime glass microscope slide to test the viability of the scanner software. From literature, [83] using laser ablation threshold data for soda-lime glass by Nieto et al.[83] for reference (For soda-lime glass, E_{th} = 2.90 J/cm^2 with a 500 fs, 1030 nm laser) laser fluence from (2.0 to 3.0 J/cm^2). These ablation thresholds are used in as the starting point of the experiment in section 4.1.2.

3.6.2 Mono-layer array laser marking

The pattern shown in **Figure 3.15** designed on the EZCAD software shown in Section **??** was marked onto the 1 μm SiO_2 mono-layer, using the UV laser system. Each numbered cell corresponding to different laser fluences starting from 2.0 J/cm^2 to 0.61 J/cm^2. And within each 'dot' of Dot code pattern, the nano-holes marked underneath the microspheres are characterised by AFM.

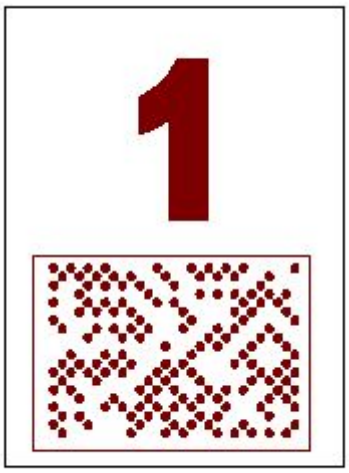

Figure 3.15 – Example of the numbered block pattern to be marked onto the mono-layer on the soda-lime glass substrate.

3.7 Theoretical work

3.7.1 XMie software

For this project, XMie was utilized in the simulation software for a dielectric particle in water or air medium, and its effect on the width and length of PNJ are investigated based on four input parameters, n_m refractive index of medium, n_p refractive index of microsphere, a particle radius and λ the wavelength of incident laser light.

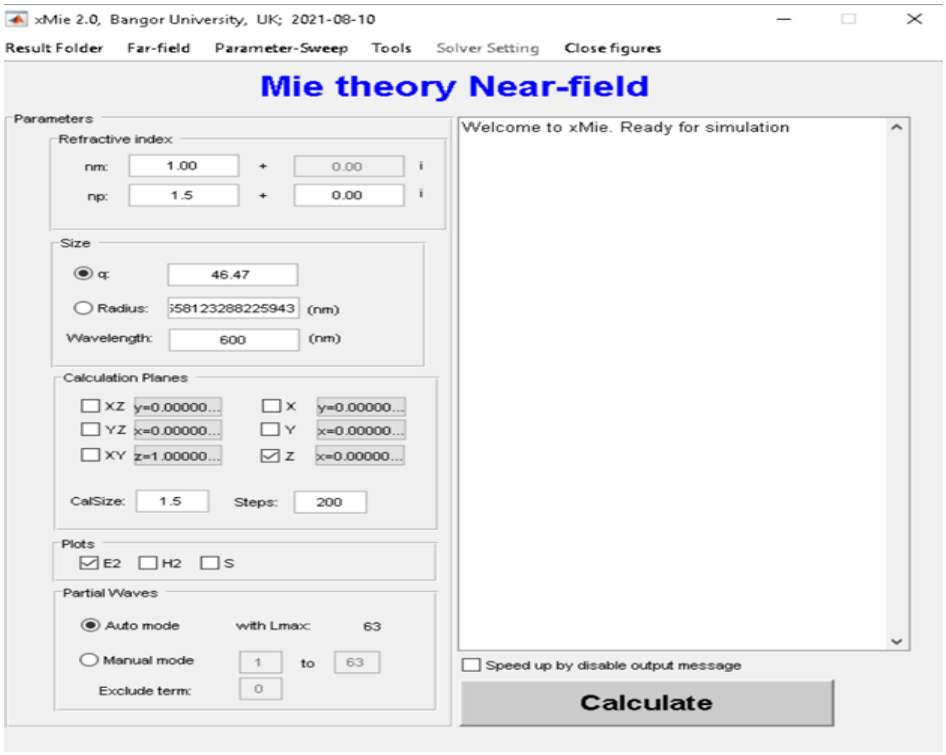

Figure 3.16 – XMie user interface

xMie is a simulation software developed by Dr Zengbo Wang, the software uses the analytical method to calculate the Mie solutions of the Maxwell's equations, for a single microsphere surrounded by a homogeneous medium under a homogeneous light source. xMie uses MATLAB as its' graphical user interface and 2D results plotting tool as shown in **Figure 3.16.** The input parameters required within the XMie user interface is n_m, the refractive index of the medium, n_p, the refractive index of the microsphere, R, radius of the microsphere, and λ, the wavelength of incident light. q is the size parameter that determines the near-field profile

of the Mie scattering effect given in Equation 3.1. The electric field intensity ($|E|^2$) results of the simulation for 1 μm in air and in water are shown in **Figure 3.17** and **3.18**.

$$q = \frac{2\pi R}{\lambda} \tag{3.1}$$

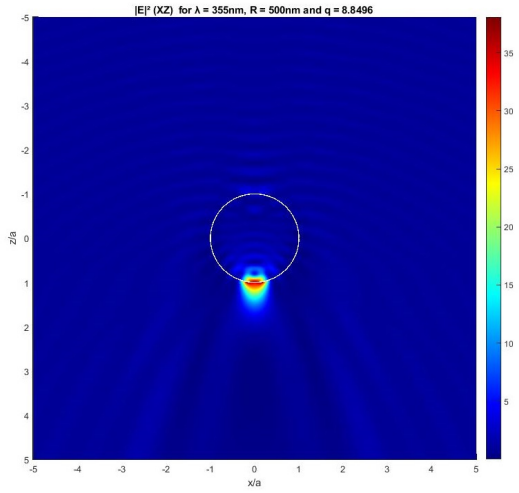

Figure 3.17 – E-field intensity $|E|^2$ of 1 μm silica microsphere irradiated by 355 nm laser in air on the XZ plane.

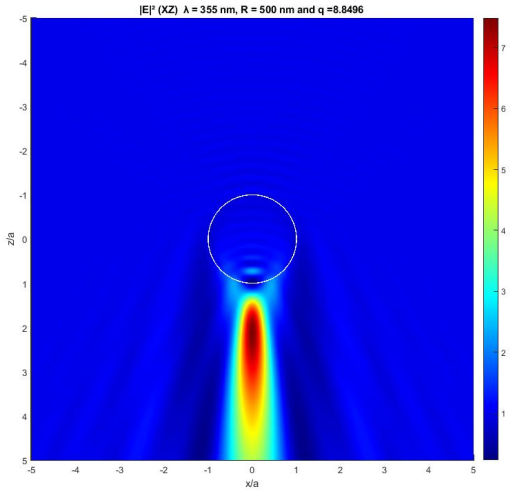

Figure 3.18 – E-field intensity $|E|^2$ of 1 μm silica microsphere irradiated by 355 nm laser in water on the XZ plane.

3.7.2 SIMULIA CST Microwave Studio Suite (MWS)

CST MWS provides multiple electromagnetic (EM) simulation solvers that uses the numerical methods such as FDTM and FIT, and simulate all types of EM phenomena onto a three-dimensional model. CST MWS was used to simulate the PNJ phenomena onto various substrates such as glass, aluminium thin film and gold to determine the focal point of the PNJ inside/onto the substrate, and estimate the size and shape of the holes in three-dimensions. The CST interface with model of the microsphere above the glass substrate is shown in **Figure 3.19** and its focusing effect in the XY plane (3.20b). XZ and YZ plane (**Figure 3.20**c and d))

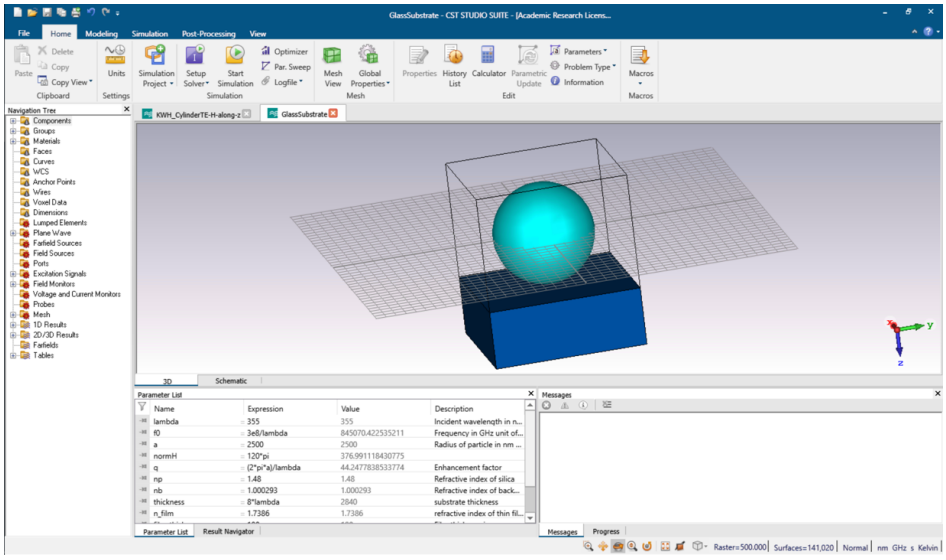

Figure 3.19 – CST User Interface

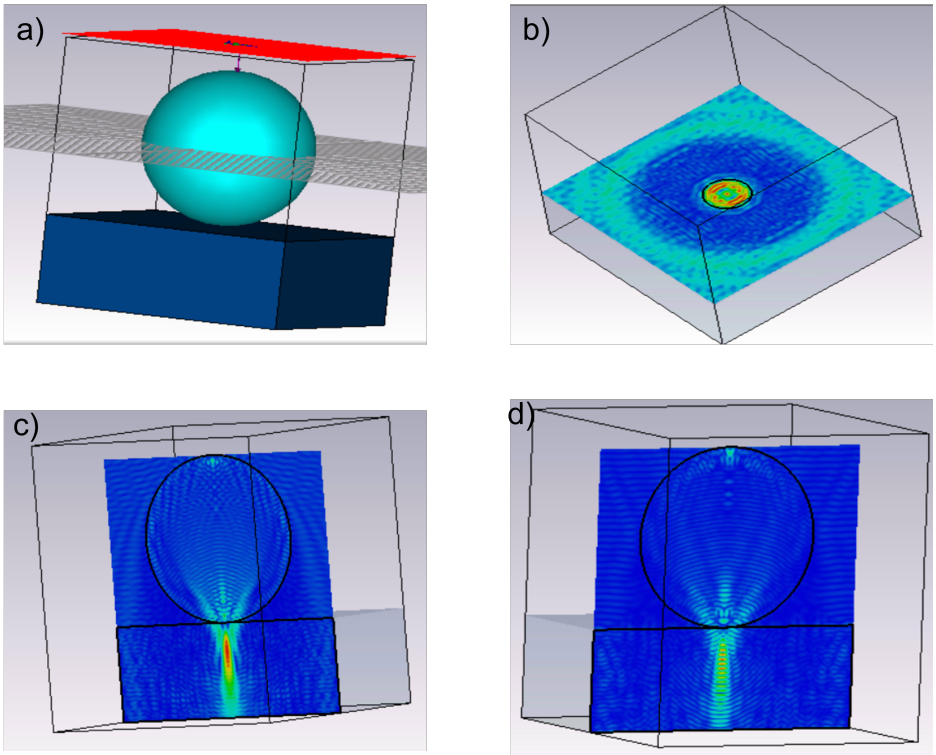

Figure 3.20 – a) 3D model of the experimental setup, red area is the incident plane wave. b) Theoretical focus points at the surface of the substrate. c) PNJ focussing effect on the XZ plane. d) PNJ focussing effect on the YZ plane.

3.7.3 Blob Detection

The fabricated patterns often requires post-processing of the microscope image in order for it to be scanned, the purpose of blob methods is to detect regions in a digital image that differ in properties, such as brightness or color, from surrounding areas. There are some properties of a blob in an image that are constant or nearly constant; all the points in a blob are similar in some sense. Therefore, attempts for blob detection using cv2.template matching to highlight locate the co-ordinates of the centre of each blob on the microscope image. The proposition for the future is to develop an automated blob detection software capable of locating the centre of the blobs and overlay a solid circle of fixed radius over it to enhance the contrast and thus the readability of the fabricated code. This process has been demonstrated manually as shown in **Figure 3.21**. This automated software has been demonstrated by [84], using iterative Laplacian of Gaussian filtering and unilateral second-order Gaussian kernels. See **Figure 3.22**.

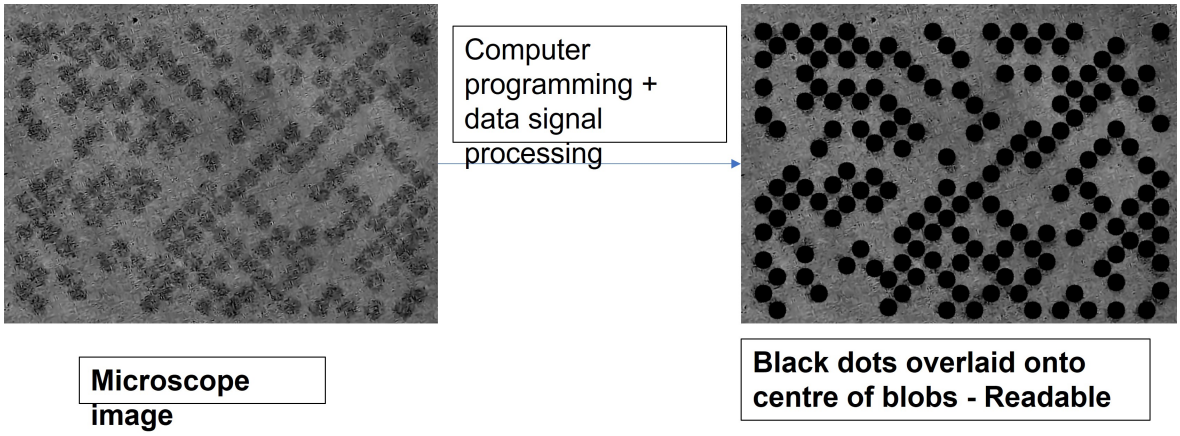

Figure 3.21 – Figure of the proposed blob detection technique.

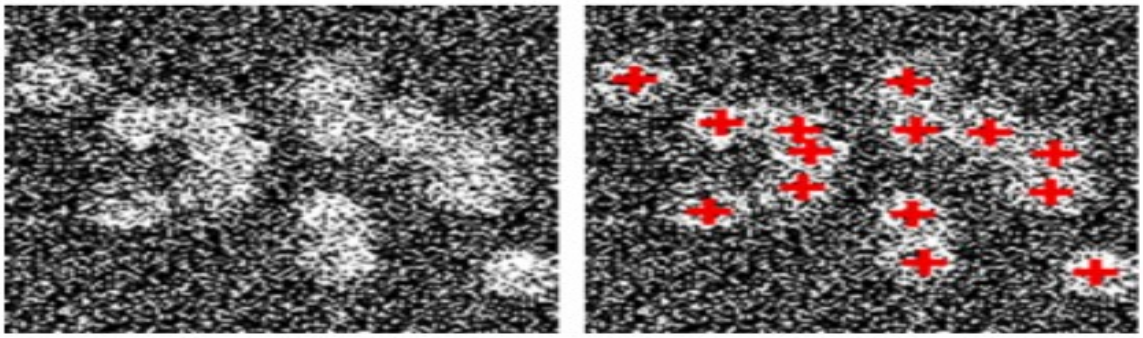

Figure 3.22 – Blob detection technique demonstrated in [84]

Chapter 4

RESULTS AND DISCUSSION

In this chapter, the fabrication time and the readability results of the 2D security codes at different sizes are compared, Dot Code was determined to be most suitable 2D code to use for application. Followed by quality of mono-layer results from the drop-casting, spin-coating and a modified Langmuir-Schaefer (LS) method, where the LS method was determined to produce suitable mono-layer quality. Nano dotocode marking assisted by superlens were then carried out and results were presented. Readout process was then discussed, followed by theoretical simulation of particle superlens focusing which supports the experiments.

4.1 Direct Laser Marking of 2D codes

We first show direct laser marking of various 2D codes without involvement of microsphere superlenses, using both UV and femtosecond lasers. From this study, we can see the marking speed, size scaling, and readout reliability advantages of dot codes over other 2D codes.

4.1.1 UV laser marking on stainless steel

Figure 4.1 (a) showns various 2D codes designs of "Bangor University" grouped in a box, including Aztec, Data Matrix, QR code, Dotcode and Barcode. They were marked on stainless steel sample in three different sizes with scaling factor, 1x, 0.5x and 0.25x (See three boxes in **Figure 4.1 (b)**). The fabrication time was recorded for each case and compared. The readability of the codes were tested by using the Barcode scanner from Section 3.3 and results are tabulated in Table 4.1 and presented in **Figure 4.2**.

From **Table 4.1** and **Figure 4.2**, the advantage of using Dot code is apparent: it performs best in terms of fabrication speed (shortest time) scalability and readability. Only Dot code can be made and successfully read out at size scaling of 0.25x when all other codes fail. The reason for this result, when scaling down, all codes except Dot code have certain degrees of patterns overlapping, leading to loss of information and thus unrecognizable by the scanner.

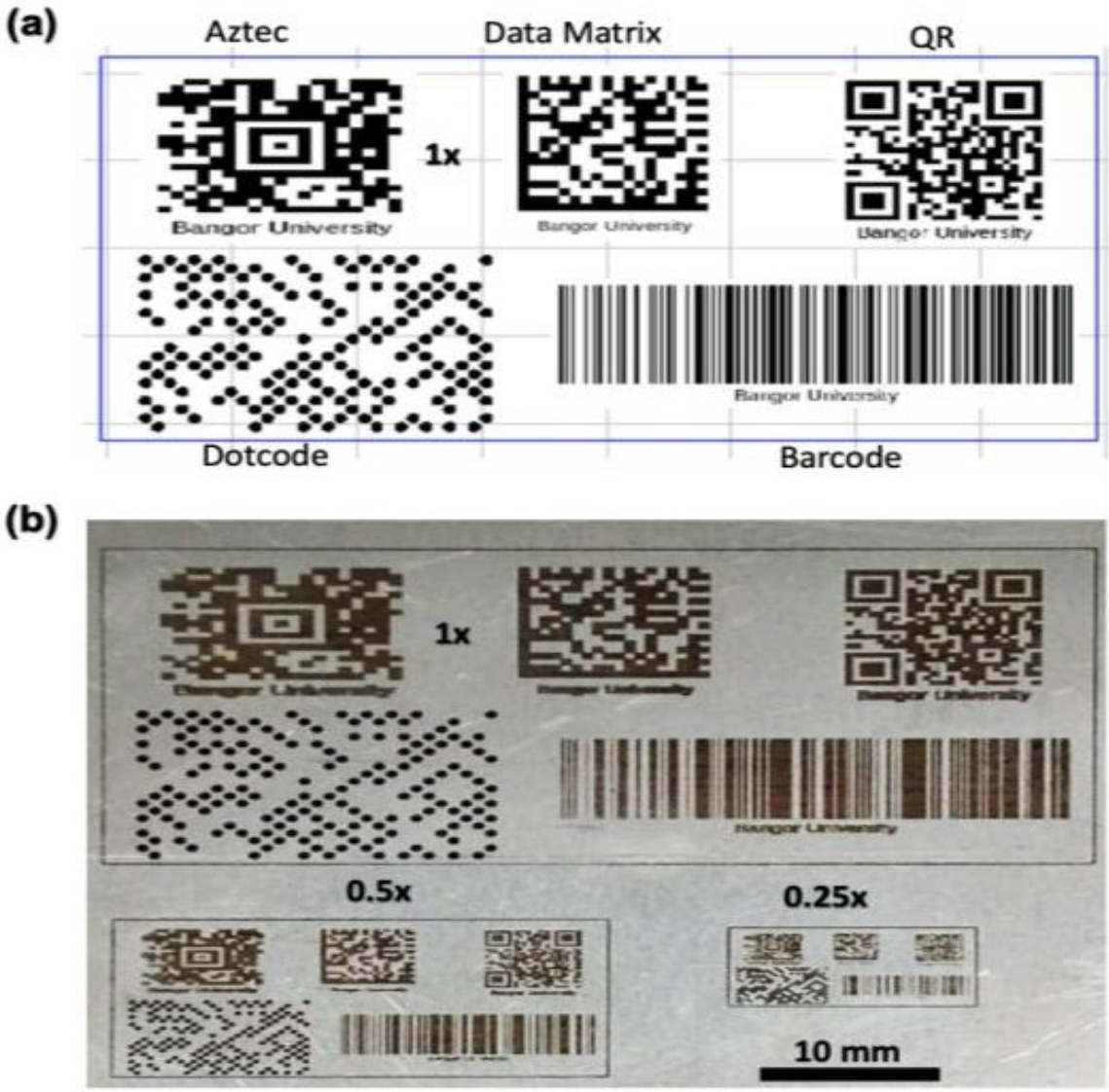

Figure 4.1 – (a) Computer aided design of 'Bangor University' 2D codes. (b) UV laser marked 2D codes on stainless steel in 3 different size scales. The scale bar is 10 mm.

In the case of the QR code, the top left and bottom left corner position alignment patterns were misaligned when marking at the smallest scale.

During laser marking, the speed of fabrication is affected by the shapes used in various 2D code schemes. In general, codes containing lines or connected squares will be slower in manufacturing, due to longer scanning path compared to the simple dot structures. Therefore, the Dot code scheme can produce fastest manufacturing speed and least manufacturing time, which is important for batch manufacturing in industrial production.

With these results, the Dot code was chosen as the most suitable code to use for further scaling down using the microsphere-induced photonic nanojet, since each 'data dot' is separated by at

2D codes	Scaling	Sizes(mm)	Fabrication times (s)	Readable?
Aztec	1x	22.086 x 20	75.06	✔
	0.5x	11.043 x 10	19.69	✗
	0.25x	5.521 x 5	4.60	✗
Data Matrix	1x	17.40 x 20	57.97	✔
	0.5x	8.710 x 10	13.28	✗
	0.25x	4.355 x 5	3.09	✗
QR code	1x	17.40 x 20	61.42	✔
	0.5x	8.710 x 10	14.91	✔
	0.25x	4.355 x 5	3.29	✗
Dot Code	1x	29.0 x 20	46.94	✔
	0.5x	14.50 x 10	11.61	✔
	0.25x	7.50 x 5	2.81	✔
Bar code	1x	42.305 x 14	105.53	✔
	0.5x	21.50 x 7	25.99	✗
	0.25x	10.576 x 3.657	5.70	✗

Table 4.1 – Fabrication speed and readability comparison of various 2D codes

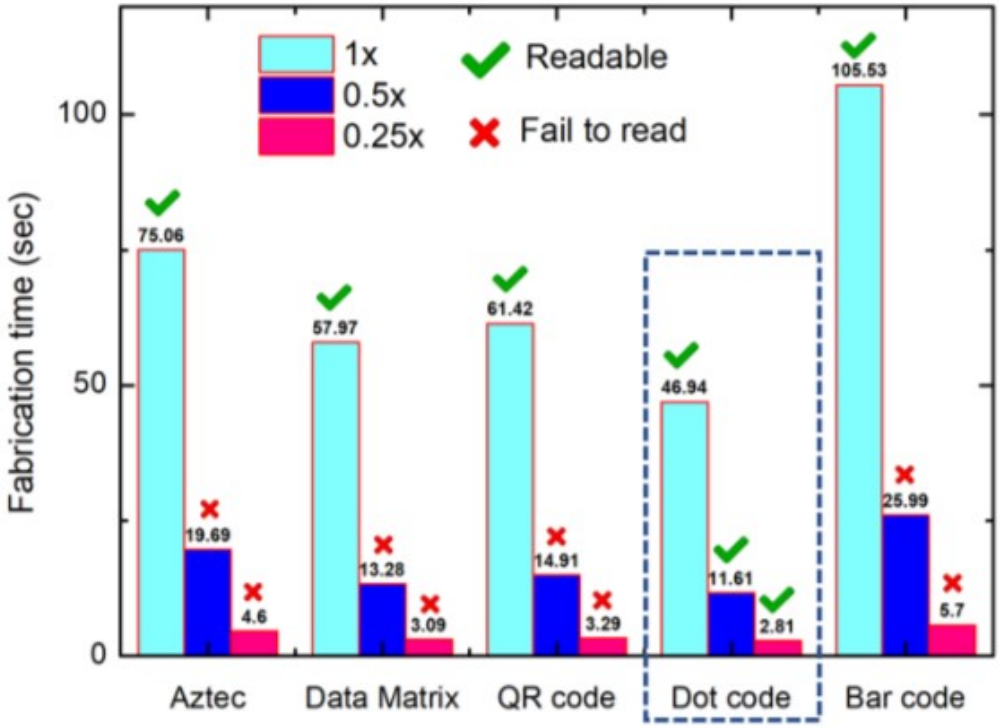

Figure 4.2 – Comparison of fabrication time (manufacturing soeed), scalability and readability of various 2D codes. Dot code has clear avantages over others: fast, scalable, and reliable.

least one empty 'data dot' space, the scanner can more easily recognise individual dots under the confocal microscope when scaled down to the micro-nano scale. All follow-on studies

will be based on Dot code scheme, including marking on glass and nanoscale marking with particle super lenses.

4.1.2 UV and FS laser direct marking of Dot code on glass

Glass is transparent to visible wavelength lasers but can be processed by ultrafast femtosecond lasers or UV lasers. Here, we performed a comparison study of direct laser Dot code marking on glass, from which we can see the advantages of using femtosecond (fs) laser in terms of its higher fabrication quality and smaller features in Dot code marking. However, fs laser system is usually much more expensive than the UV laser system. From collaborating company Light Future Ltd.'s point of view, while they wish to understand the advantages of fs laser, they prefer further development of the project to be focused on UV laser system to minimize the overall system cost. **Figure 4.3** shows the Dot code "Bangor" directly fabricated on

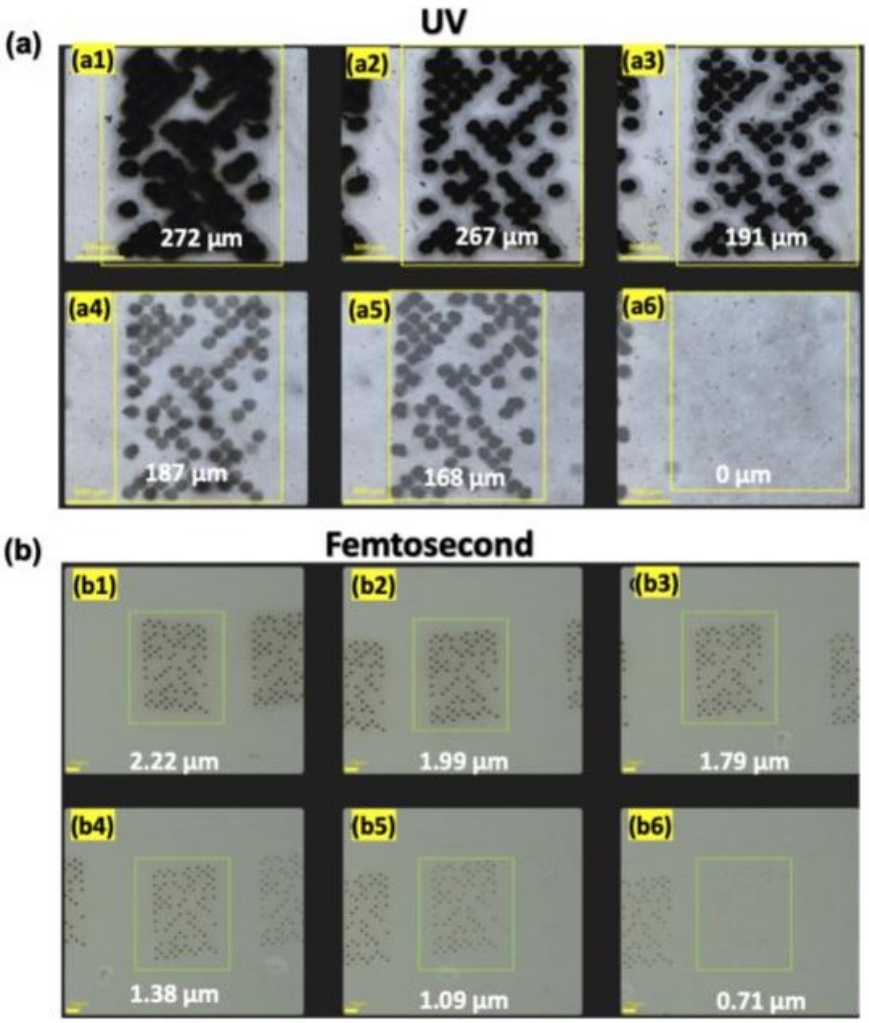

Figure 4.3 – UV and femtosecond laser marking of Dot code "Bangor" on glass. (a1 - a6) UV laser at laser fluences of 5.2, 4.6, 4.1, 3.5, 2.9, 2.0J/cm^2 respectively, (b1 - b6) Femtosecond laser at fluences of 2.6, 2.4, 2.2, 1.8 1.5 J/cm^2 respectively. The corresponding feature sizes of each tested laser fluence in μm are displayed at the bottom of each figure.

soda lime glass withgout using particle superlens by both UV and fs lasers and the average feature sizes under a range of laser fluences. It clearly shows higher quality and much smaller patterns can be formed by fs laser shown in (b) compared to the UV laser patterns shown in (a). Subwavelength nanoscale marking by fs laser. with hole size 0.71 μm, is demonstrated in **Figure 4.3 (b6)**. Such hole size is below the fs laser wavelength of 800 nm. UV laser marking shows much larger and lower quality dot holes. At fluences below threshold, the dot holes are non-existent on the surface **Figure 4.3 (a6)**.

There are several reasons for this: First, the used UV laser system has a low NA (NA = 0.15) focusing lens, while the used fs laser system has equipped with higher NA (NA = 0.65) objective lens. The UV scanner cannot perform single dot marking so each dot is enlarged to a size which can be produced by circular scanning. Second, fs laser ablation of glass is due to nonlinear multiphoton absorption effect where the heat effect is minimized with almost negligible heat affected zone (HAZ). Thirdly, the fs laser is equipped with precision imaging system so that the focus positioning is much accurate than the UV laser system without focusing imaging system. Again, from industrial standpoint, it is preferred for the final system to be more robust to the variation in focusing position during manufacturing process, and low-cost. It is thus decided all follow-on studies on particle superlens will be using UV laser instead of fs laser. However, future work on using femtosecond laser will be beneficial to expanding this marking technique on other substrates.

4.2 Fabrication of large area superlens array

In our proposed superlens-assisted marking technique, a large-area array of microsphere superlens is required. The array should be in monolayer form to enable particle focusing. Multilayered particles are likely to change particle focusing and affect the marking process so we need to avoid. We thus need to prepare and obtain reasonable quality large-area monolayer particle lenses before laser marking, with multilayered particles as little as possible.

In this project, we have tested and compared three different preparation methods, i.e., drop-casting, spin-coating and modified Langmuir Schaefer (LS) which are shown below. Among them, the modified Langmuir-schaefer method produced the best balanced large-area monolayer result and is thus selected and used for the follow-on experiments, which are performed on glass substrate.

4.2.1 Drop-casting method

Figure 4.4 shows a 1.0-µm-SiO^2 particle array prepared on glass substrate of size approximately 1 cm in diameter by drop casting method (see details in Section 3.5.1 in Chapter 3 - Methodology). As it can see, the particle array has a poor quality, with very uneven distribution and particle aggregations. Such quality of particle lenses is not suitable for our proposed application. It might be possible to improve the quality by using other liquid solvent [85] and [86], instead of water, and with additional substrate surface pre-treatment. However, it is unlikely that a large-area if the ideal conditions the reliability of this approach is in doubt due to the variations in concentration of microspheres inside the droplet and evaporation rate differences between the outer edge and the bulk of the droplet, may cause the variations in the quality of the mono-layer.

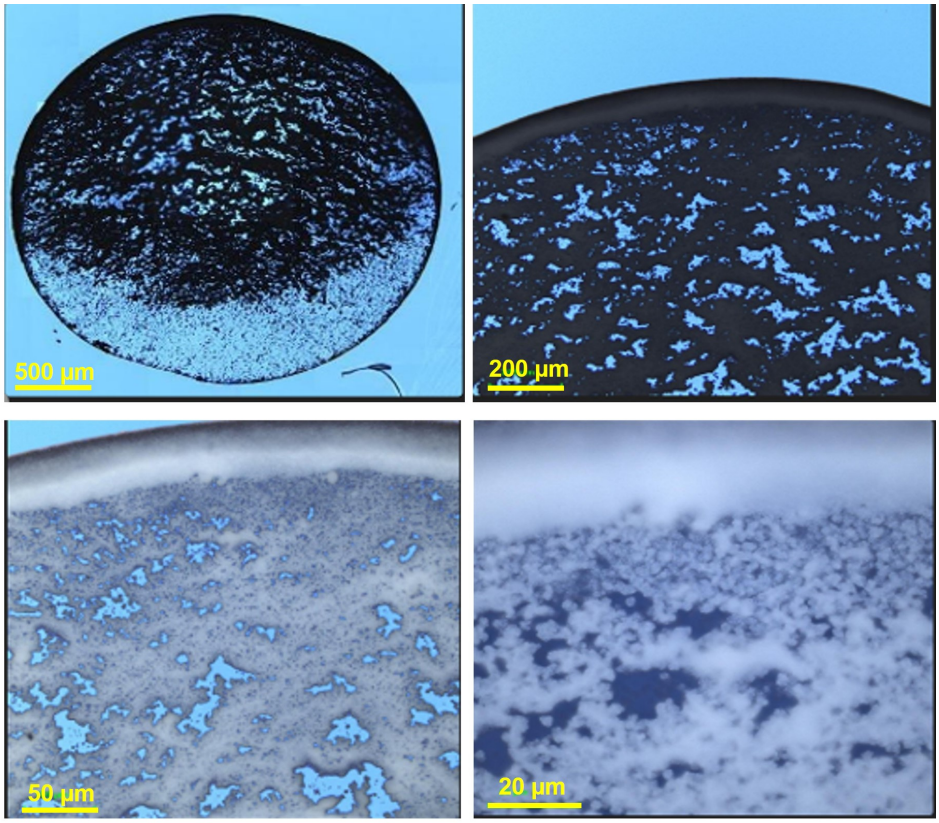

Figure 4.4 – Confocal microscope images of silica microsphere deposit using drop-casting method on glass substrate, from 5x to 50x magnification. (The scale bars are 500, 200, 100, 50, 20 μm respectively.)

4.2.2 Spin-coating results

The spin-coating results is shown in **Figure 4.5**, this approach shows some regions of monolayers with many areas of aggregations, from further investigation on the mechanisms of

colloidal self-assembly into Toolan et al. [87], where the direct observations of the self-assembly of latex colloids during spin coating were conducted, and identified several factors that were previously not considered, in summary, the choice of using water as the solvent, low concentration ($\approx 10\%$) and the low spin speed and time relative to the size of the particle have all been shown to have a detrimental effect to the quality of the mono-layer. Spin-coating offers rapid deposition of the mono-layer onto an arbitrary substrate, however, the multiple underlying mechanisms including the properties of the solvent, substrate and the microsphere , spin speed and time requires rigorous testing that may be very time consuming.

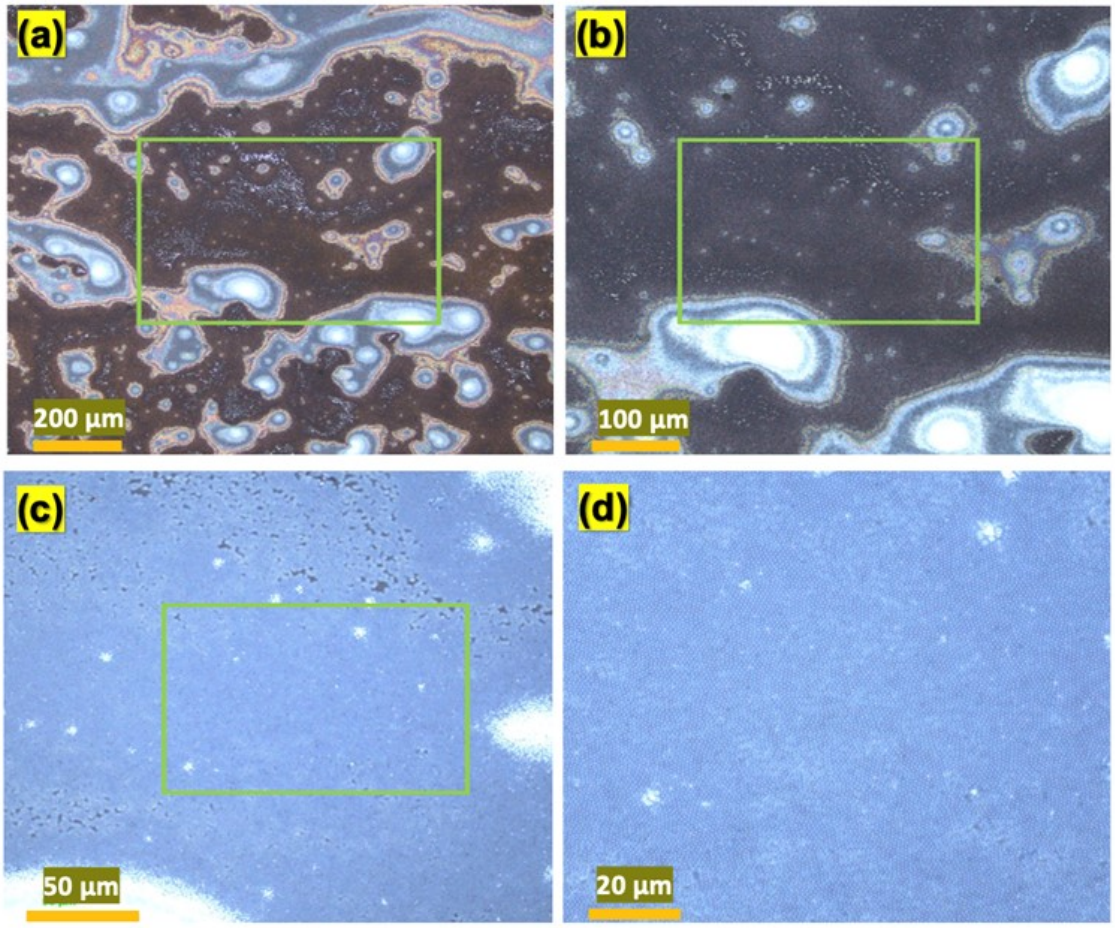

Figure 4.5 – Spin coating of 1.0 μm SiO_2 microspheres on glass substrate. Magnifications: (a) 10x, (b) 20x, (c) 50x, (d) 100x.

4.2.3 Modified Langmuir–Schaefer (LS) method results

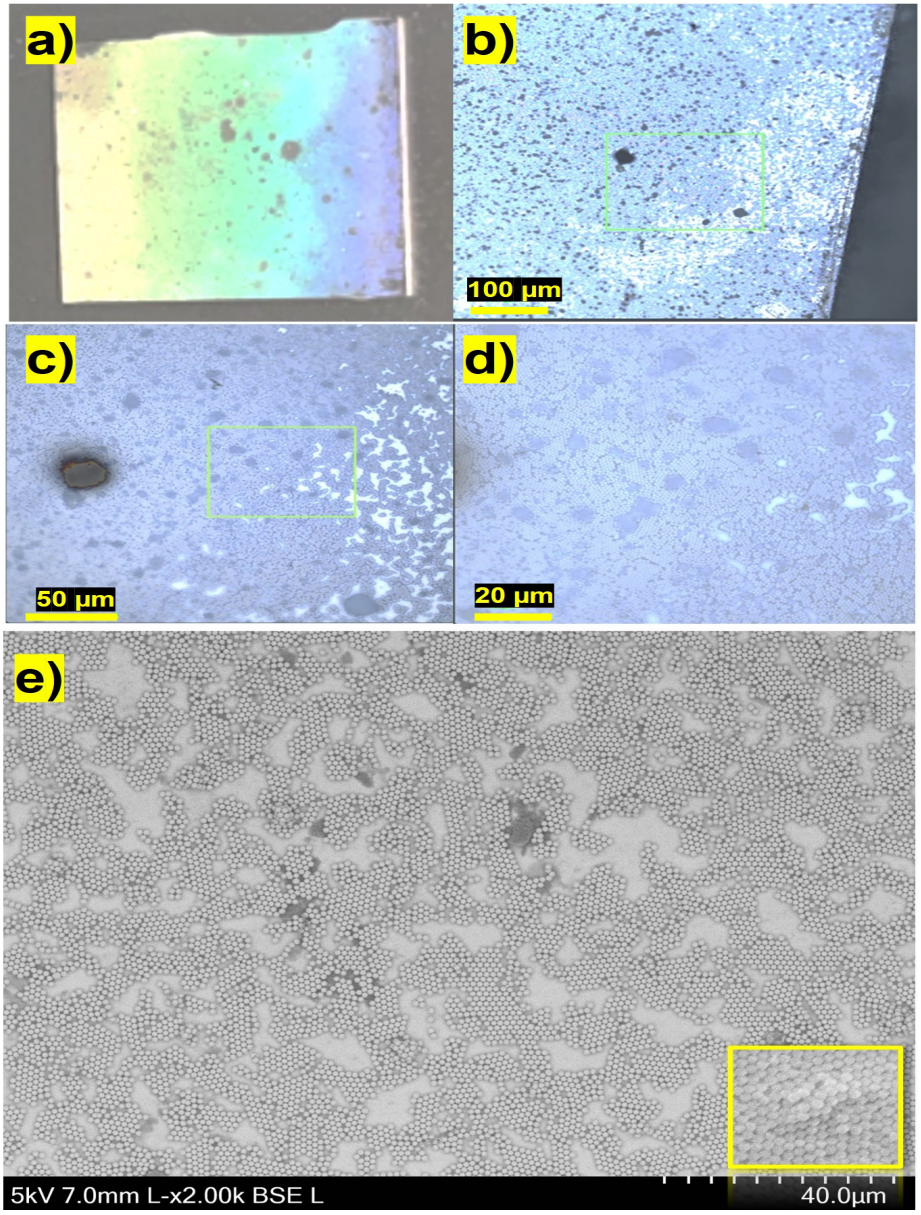

Figure 4.6 – Optical images of the modified Langumir-Schaefer (LS) assembly of microspheres on glass surface. (a) Photograph of overall large-area view, (b) 10x, (c) 20x, (d) 50x, and (e) SEM image of monolayer. The inset shows multilayer aggregates in some regions.

The results of the MLS method have shown to be the most suitable method of depositing the silica microspheres monolayer. As shown in SEM image in **Figure 4.6**, the monolayer quality is reasonably good, covering majority area of the sample surface. The gap zones of uncovered particle area are roughly between 4-20 μm, smaller than the laser spot size of about 50 μm. This is important to ensure that within each laser processed spot there will be microsphere super-lenses presented for the nano-marking process. If the gap spot size is larger than the laser spot size and there are no particles within the laser spot, the technique

will fail. Therefore, owing to the simplicity and cost of the setup and acceptable fabrication time of the MLS technique, all Dot code laser marking experiments in later sections were chosen to proceed with the MLS deposition technique.

Ideally, the mono-layer is highly ordered and covers all areas which can be optimised as future work of the project. However, the current mono-layer quality with gap size below laser spot size is sufficient to demonstrate our key concept on superlens-assisted Dot code nanomarking.

4.3 Superlens-assisted Dot code marking

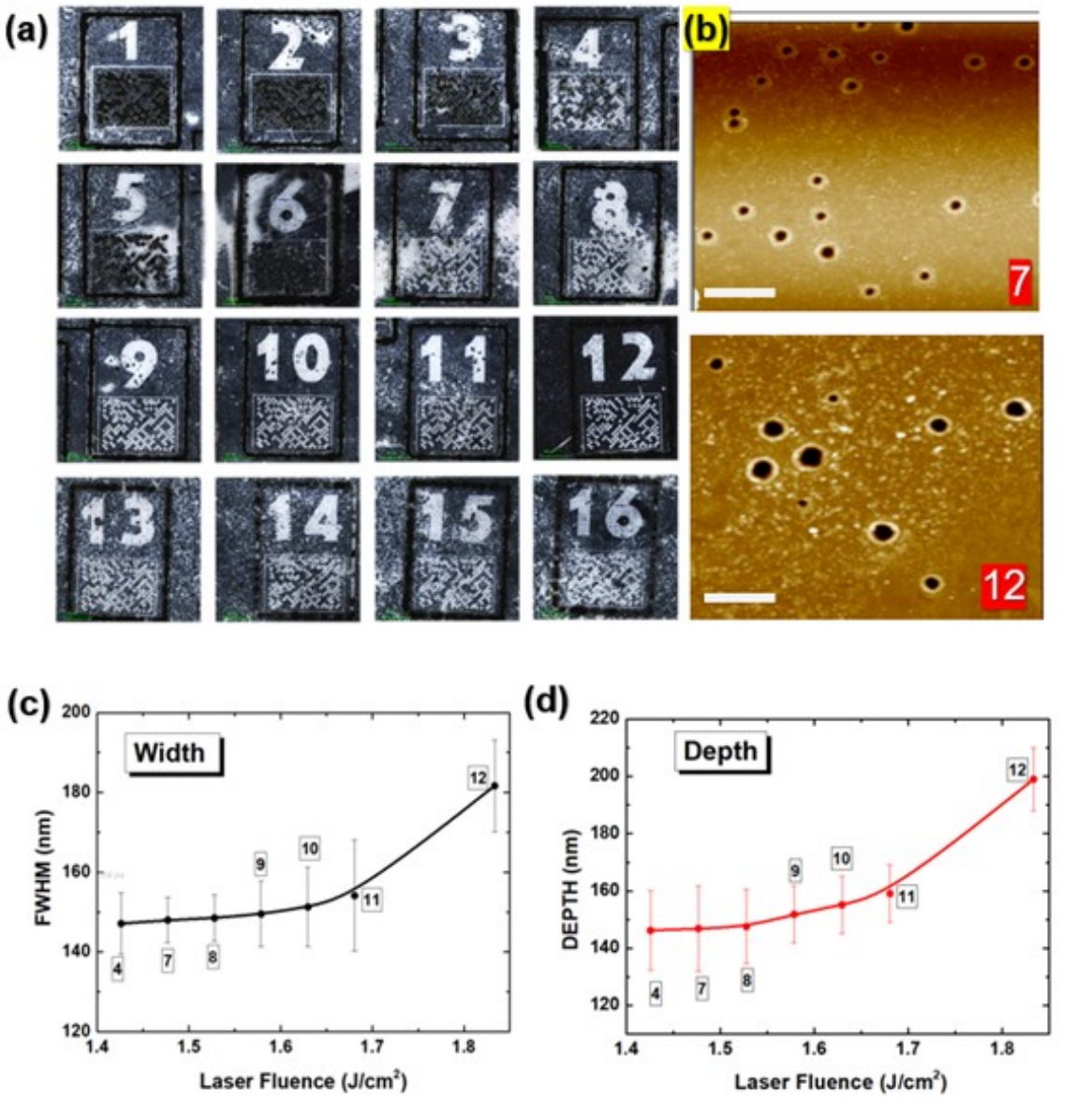

Figure 4.7 – Superlens assisted Dot code nano marking by UV laser. (a) Overview of the Dot code marking at 16 different laser fluences. (b) AFM images of nanoholes for No. 7 and No. 12 block. (c) Width of nanoholes measured at Full width at half maximum (FWHM). (d) Depth of nanoholes. Scale bar: 500nm.

Figure 4.7 shows the fabricated samples after laser marking of Dot code "Bangor University" with particle superlens on top at different laser energy levels, with laser fluences decreasing from $\sim$ 2 J/cm^2 (block 1) to $\sim$1.43 J/cm^2(block 16) with step $\sim$0.05-0.06 J/cm^2. The resulting blocks could be divided into several groups:

Group 1: Blocks 1, 2 and 3. These three blocks have similar patterns with a black-out appearance. This is due to the high laser fluences used in these cases (1.986 J/cm^2, 1.935 J/cm^2, 1.884 J/cm^2), all particles were removed, and conventional laser ablation were then taking place, thus leading to the formation of micro-sized holes at each processed spot and therefore, will not contain the nanoscale holes desired as illustrated in **Figure 1.1**. Thus, group 1 were omitted from further AFM analysis. As shown above in Section 4.1.2 - **Figure 4.3**, if there are no particle super-lenses on top, the sample won't be processed by UV laser as it is slightly below the ablation threshold fluence of 2 J/cm^2. Therefore, the presence of microsphere superlens helped to reduce the ablation threshold, due to focusing effects by microsphere lenses, which will be explained by theoretical results in following section 4.5.

Group 2: Blocks 4,5 and 6. Block 4 is bit abnormal, while blocks 5 and 6 looking similar to Blocks 1-3. In theory, block 4 should be having a black-out appearance as well following the simple laser energy decreasing tendency, since blocks 1-3 and 5-6 all having same blackout appearance. We attribute the abnormality of block 4 to the possible variation and fluctuation of laser and processing systems, and therefore block 4 and 5 were also omitted from further AFM analysis and this range of laser fluences should be avoided in industrial settings where process stability and repeatability are key requirements.

Group 3: Blocks 7-12. These blocks are most well defined, with strong contrast between laser processed (white area) and non-processed areas (black area). They can be easily readout by the Scanner APP with remaining particles not cleaned. This is the range of processing parameters we should recommend to use in industrial setting, which stable and repeatable. Here, each laser processed spot contains a cluster of nanoholes, which are generated by particle superlens. Under each particle superlens, a nanohole will be generated. An example was shown in **Figure 4.7(b)** for block 7 and block 12, where the nanoholes are about 180 nm and 150 nm, respectively. Note the hole size within each block could vary due to a number of factors: energy variation in a laser spot at different particle locations, inhomogeneity of

laser focus etc. The measured nanohole width at Full-Width-at-Half-Maximum (FWHM) and depth are summarized in **Figure 4.7 c and d)**, where the error bars demonstrating the size variations of about 10-20 nm. A general tendency can be observed: both width and depth of nanohole increases with laser fluences. The is easily understandable since less energy leading to less material removal within the particle focusing spot which is in contacting with sample surface (as shown below by theoretical calculation).

Group 4: Blocks 13-16: these blocks are similar to blocks 7-12, but with reduced dotcode pattern clarity and contrast. They are still acceptable for the nano-marking process and is expected to have smaller nanoholes. Depending on end user needs, this range of parameters may be used if smaller nanoholes is preferred. The reduced contrast proven to be too difficult for the barcode scanner to readout the dot code under the microscope image and thus, these blocks were not analysed in depth in comparison to Group 3 (Block 7-12)

Smaller laser fluences beyond block 16 (1.17 J/cm^2) were also studied, those samples contain almost invisible microscope images and are thus not very meaningful in terms of optical readout. These results were not presented.

4.4 Blob detection and readout

We now turn to the final readout stage of laser marked Dot codes from cleaned samples. The left particles were removed by cotton wipes and followed by DI water rinsing and drying. Due to the sparse distribution (non-connected) nature of Dot code blobs, the sample has low visibility in general under naked eyes, most patterns are invisible to the eyes and microscope imaging is required to clearly reveal the patterns. **Figure 4.8** shows captured confocal microscope images of the cleaned samples. As shown in **Figure 4.8 a)**, the dotcode pattern is sharp and clear, and in high contrast for block 2 (similar for group 1: blocks 1-3) when laser fluence is high, which can be easily readout by the scanner APP. However, such patterns are not what we aim for since they did not contain nanoscale features required for the second level security protection. In contrast, **Figure 4.8(b)** shows the final dotcode pattern for block 12 within recommended fluence ranges for nanomarking. Here, each blob within the dotcode consists of a group of nanoholes, as shown by AFM analysis in previous section in **Figure 4.7**. Comparing with Fig.4.4(a), the contrast of nanoholes is lower because each blob consists of sparse nanoholes. The reduction of contrast makes patterns less visible which

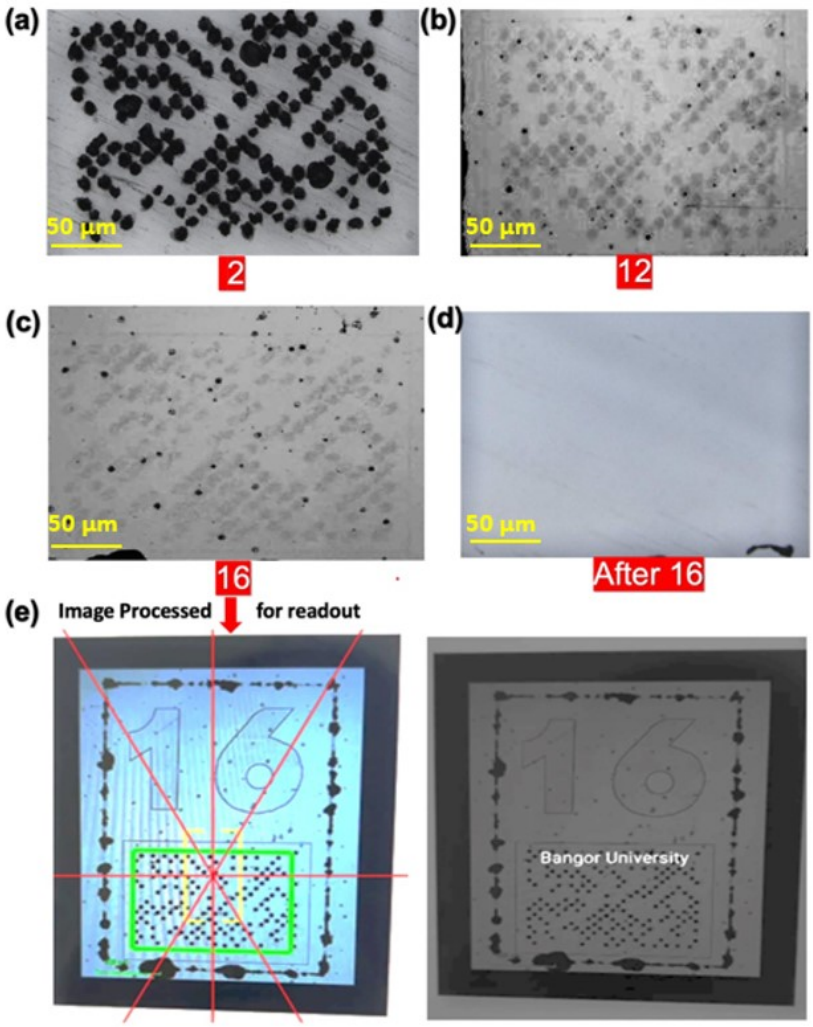

Figure 4.8 – Cleaned samples after superlens-assisted laser marking. (a) Block 2, high energy, single dot in microscale, no nanoholes within each spot. (b) Block 12, Medium energy, reasonable contrast Dot Code with nanoholes within each spot. (c) Block 16, low energy, reduced contrast Dot code with nanoholes within each spot. (d) No visible Dot code on surface for lower energy marking. (e) Imaging Processing of Block 16 in (c) for successful readout.

offers higher level security protection. Variations of contrast between blobs in **Figure 4.8 b)** are attributed to the variations in nanoholes size, depth, and density within that blob, causing by various reasons including laser beam inhomogeneity and monolayer quality in that blob. When laser fluences drop further (group 4: block 13-16), the nanohole size and depth reduce accordingly, leading to the lower contrast as observed in **Figure 4.8 c)**. Further reduction of laser fluences leads to no nanoholes on surface as shown in **Figure 4.8 d)**.

In most cases the nanohole-decorated dotcode patterns (**Figure 4.4 b and c**) cannot be directly readout by the scanner APP due to insufficient contrast level with respect to its background.

Image processing is thus required, either to improve the contrast to a sufficient level for readout, or to retrieve the blob positions and replace the blob with an artificial black dot.

4.5 Theoretical study of superlens focusing

The physics behind current technique is quite clear: particle superlens generates highly focused nano focusing spot at sample surface, which leads to the formation of nanoholes when coupled to a pulsed UV or femtosecond laser source. In this section, we show simulated light focusing by particle lens by using both xMie (No substrate case) and CST (with glass substrate) software to support and explain the obtained experimental results. Two cases were considered, single particle and aggregated particles.

4.5.1 Single particle

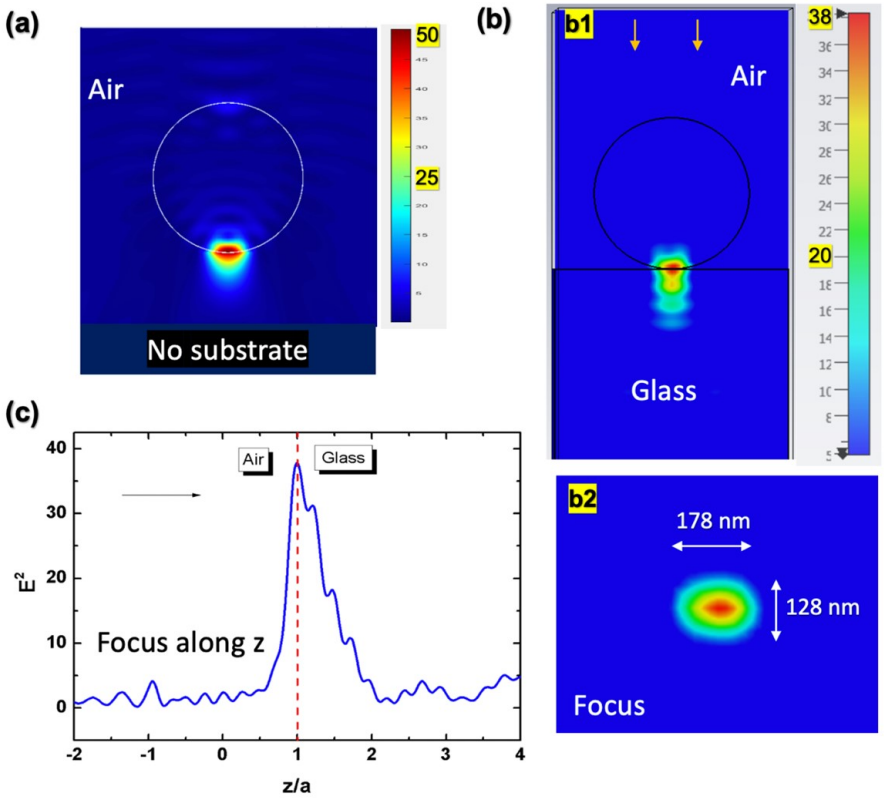

Figure 4.9 – Theoretical calculation of single particle lens focusing by xMie and CST. (a) E2 field distribution of a single particle in air without substrate, calculated by xMie software. (b) E2 field distribution for particle on glass surface, calculated by CST. (b1) side view (b2) top view of focusing on substrate surface. (c) E2 field profile along z-axis in propagation direction. Peak focus at particle-substrate contacting point with enhancement factor of 38.

When light interacts with a single microsphere, Mie theory can be used to calculate the exact field distributions around the particle lens. **Figure 4.9 (a)** shows calculated E^2 intensity field by in-house developed xMie software around a 1 μm SiO2 microsphere in air. Note in this case there is NO substrate. The focus point is right at the bottom of the particle, with a

peak enhancement value of 50. In case of particle on surface, Mie theory cannot be used and instead a numerical software CST was used. **Figure 4.9** (b) shows calculated E2 field distribution for a 1μm SiO^2 particle on glass surface, (b1) side view and (b2) top view of focusing on substrate surface. Here, one can see the focus is still located at the contacting point when the substrate is presented, but with reduced peak enhancement value of 38. The reduction of focus enhancement is caused by the efficient coupling of laser energy from microsphere lens into the glass substrate which is transparent to the laser beam. In contrast, if the substrate is not transparent to the incident beam, for example a metal substrate, the presence of substrate could lead an increased focus intensity due to reflection [88]. From **Figure 4.9 (b2)**, we can see the simulated focus spot size on sample surface beneath the particle is about 178 nm x 128 nm measured at FHWM, which is NOT a perfect circle but in an elliptical shape. This can be verified from experimental results in Fig. 4.3, where most nanoholes are bit elliptical. The size of nanoholes obtained in experiments is generally smaller than 180 nm which agrees with the theory. **Figure 4.9** (c2) shows calculated focus intensity along z-axis (the propagation direction), which manifests a rapid decay within one radius distance (500 nm). In other words, the theory predicts the depth of all nanoholes wi ll be less than 500 nm. At experimental fluences ranges, the depth of nanoholes is about 200 nm and below, which is within the predicated depth zone.

4.5.2 Aggregated particles

In experiments, the self-assembled particle superlens array is not in perfect monolayer form, they have defects including gaps and aggregates, both will affect the focusing. To demonstrate these effects, we studied a simple two-layered particle system as shown in **Figure 4.10**, where the first layer has three particles and second layer has two particles. All other simulation settings are same to that in the **Figure 4.9** case above. From **Figure 4.10**, we can observe:

1. Particles sitting at the edges of an array (first layer) will have stronger focus compared to those sitting in the middle (see **Figure 4.10 b and c**).
2. Particles in the second layer does not contribute to nanohole generation on sample surface, despite they produce strong focus right beneath themselves.

These theoretical effects, again, are important in guiding and explaining experimental findings during the project, where nanohole variations occur and there are very few nanoholes generated

under aggregated particles. In view of **Figure 4.10**, the theoretical work has provided a very useful insight and support to the experimental work carried out in the project.

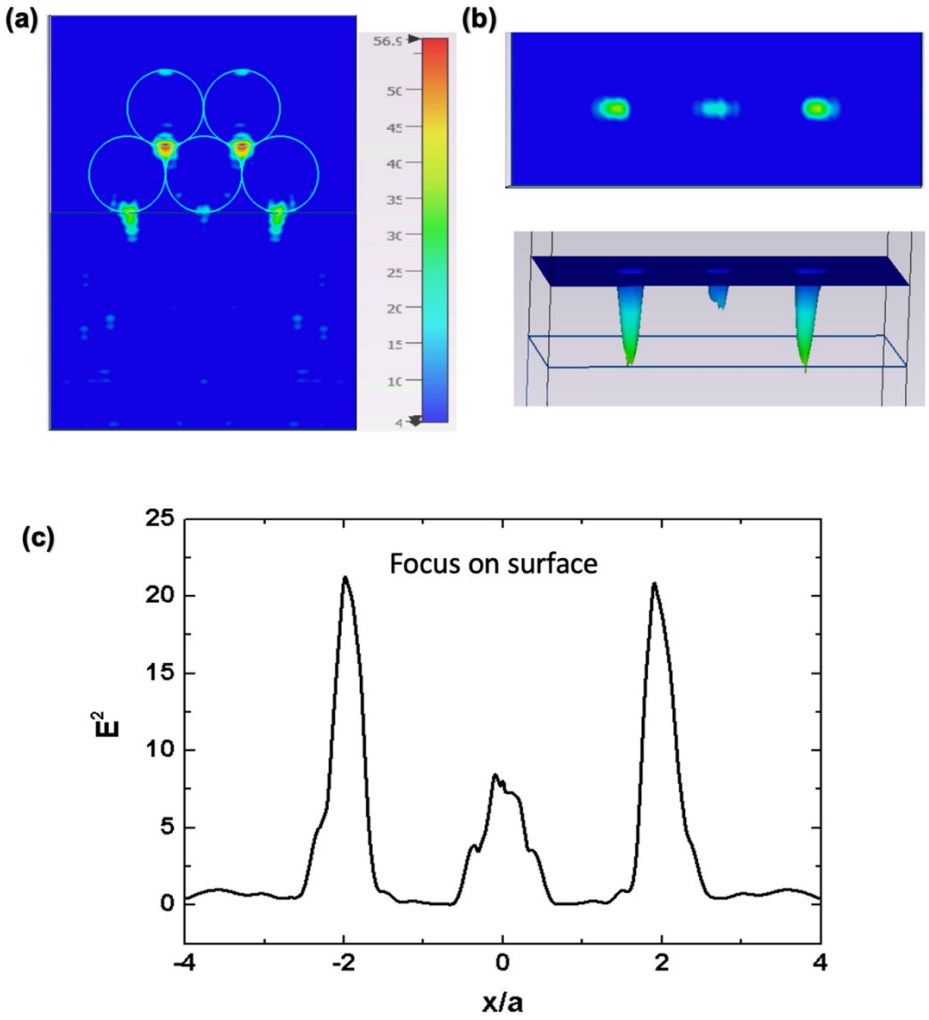

Figure 4.10 – Focusing affected by particle aggregation states. (a) E^2 intensity distribution within XZ cross-sectional plane for 5 particles aggregated in two layers (b) Focus spot on sample surface, 2D distribution (c) 1D intensity profile along x-axis on sample surface showing different focusing under particles.

Chapter 5

CONCLUSION

5.1 Conclusions

We have developed a new laser-based anti-counterfeiting technology in this project. It is based on the novel concept of using particle superlens to generate subwavelength nanoscale holes within each laser processing spot, providing a second level of security protection over conventional laser marking. When combined with DotCode scheme, the final obtained security Dotcode marking is highly security and different to be copied by other counterfeiters. Key scientific conclusions are:

- DotCode scheme is ideal for high level security protection. Compared to other 2D code schemes, this project shows it is one of the simplest, easiest, and fastest to manufacture and scaling down coding schemes.
- Microsphere particle superlens can focus incident laser beam into nanoscale spot size, allowing sub-wavelength patterns like nanohole to be generated under the particle lens. With 1 mm SiO_2 microsphere used in the project and under a UV laser source (355 nm), the fabricated hole size (FWHM) is about 140-180 nm for most cases, with features size below the diffraction limit size of half wavelength of 178 nm. When particles were used in array form, an array of sub-wavelength nanopatterns were successfully generated.
- Combining DotCode scheme with microsphere superlens nano focusing capability leads to the successful demonstration of proposed superlens-assisted anti-counterfeiting laser Dot code marking technology, which can be applied onto almost all materials including glass, stain steel, diamond, precious gems, and luxury goods. The final obtained nanomarking are invisible to human eyes. Readout of these nano Dot code patterns would require microscope imaging and advanced imaging processing, making them less possible to be copied.

5.2 Future Work

Alongside present work, following future work are recommended:

1. A higher quality monolayer particle array. Despite the efforts in this project and a reasonable quality of particle monolayer has been achieved across a large area in centimeter scales. The monolayer still contains obvious gap zones and multilayer aggregations. Ideally these defects will be removed in future by further optimizing the monolayer preparation method such as controlled humidity and liquid flow in MLS technique.
2. Application on other materials. Due to the time limitation of this project, the demonstration has been limited to glass and stainless materials. However, the technique can be easily applied to almost all material where the material can be laser ablated by UV laser wavelength. Successful trials on diamonds have been performed. However, those results will be kept as confidential commercial sensitive information so won't be able to be included in current thesis. The company has plan to apply the technique to precious gems and luxury goods.
3. Reuse of particles. Microspheres used in this project are relative expensive, so reuse of the particles are important to save the costs. In principle, there are no damage to microsphere during laser marking process despite they can be removed from sample surface. All particles can be collected and reused by appropriate recycling process. Another idea is to encapsulate the particle monolayer in a transparent host medium to form a film-like particle lens, which can be directly placed on top of sample surface and reuse it many times. More efforts are needed on these proposals.
4. More advanced blob detection algorithm. Currently our blob detection program stops working at certain contrast level. Pushing such limit with more advanced blob detection algorithm is of great interest to the project.

Sponsorship

Mae'r Ysgoloriaeth Sgiliau Economi Gwybodaeth (KESS 2) yn fenter sgiliau lefel uwch Cymru gyfan a arweinir gan Brifysgol Bangor ar ran y sector AU yng Nghymru. Fe'i cyllidir yn rhannol gan raglen cydgyfeirio Cronfa Gymdeithasol Ewropeaidd (ESF) ar gyfer Gorllewin Cymru a'r Cymoedd. Knowledge Economy Skills Scholarships (KESS 2) is a pan-Wales higher level skills initiative led by Bangor University on behalf of the HE sector in Wales. It is part funded by the Welsh Government's European Social Fund (ESF) convergence programme for West Wales and the Valleys.

References

[1] K. Srivastava, 'Fake covid vaccines boost the black market for counterfeit medicines,' *bmj*, vol. 375, 2021 (p. 3).

[2] S. Bonev and B. Wirnitzer, 'Security printing for product packaging in industrial printing applications,' in *Proceedings of 35th International Research Conference of IARIGAI*, 2008 (p. 3).

[3] M. Chandak, P. Shinde and D. Raut, 'Process parameter optimization for laser 2d barcode engraving using taguchi design of experiment technique,' *International Journal of Engineering Research & Technology*, vol. 9, no. 11, pp. 263–267, 2020 (p. 3).

[4] K. D. Kanev, P. V. Gnatyuk and V. A. Gnatyuk, 'Laser marking in digital encoding of surfaces,' in *Advanced Materials Research*, Trans Tech Publ, vol. 222, 2011, pp. 78–81 (p. 3).

[5] X. Li, L. Yang, B. Chang *et al.*, 'Simulation and process optimization for laser marking of submillimetre rasterizing 2d code on stainless steel,' *International Journal of Modern Physics B*, vol. 34, no. 28, p. 2 050 266, 2020 (p. 3).

[6] C. Archambeau, *Anti-counterfeiting technology guide*. [Online]. Available: `https://euipo.europa.eu/tunnel-web/secure/webdav/guest/document_library/observatory/documents/reports/2021_Anti_Counterfeiting_Technology_Guide/2021_Anti_Counterfeiting_Technology_Guide_en.pdf` (p. 6).

[7] X. Li, Z. Chen, A. Taflove and V. Backman, 'Optical analysis of nanoparticles via enhanced backscattering facilitated by 3-d photonic nanojets,' *Optics express*, vol. 13, no. 2, pp. 526–533, 2005 (p. 9, 29).

[8] W. Jangsombatsiri and J. D. Porter, 'Laser direct-part marking of data matrix symbols on carbon steel substrates,' 2007 (p. 9).

[9] A. Longacre Jr and R. Hussey, *Two dimensional data encoding structure and symbology for use with optical readers*, US Patent 5,591,956, Jan. 1997 (p. 10).

[10] B. Furht, *Handbook of augmented reality*. Springer Science & Business Media, 2011 (p. 11).

[11] T. Li and K. D. Messer, 'To scan or not to scan: The question of consumer behavior and qr codes on food packages,' *Journal of agricultural and resource economics*, vol. 44, no. 1835-2019-1549, pp. 311–327, 2019 (p. 11).

[12] K. Berisso, 'Dotcode damage testing,' *Journal of Computer Sciences and Applications*, vol. 6, no. 1, pp. 43–47, 2018 (p. 12).

[13] I. S. Reed and G. Solomon, 'Polynomial codes over certain finite fields,' *Journal of the society for industrial and applied mathematics*, vol. 8, no. 2, pp. 300–304, 1960 (p. 12).

[14] S. Ikuta, 'Multimedia-enabled dot codes as communication technologies,' in *Advanced Methodologies and Technologies in Media and Communications*, IGI Global, 2019, pp. 263–276 (p. 12).

[15] M. Hong, S. Huang, B. Luk'yanchuk and T. Chong, 'Laser assisted surface nano-patterning,' *Sensors and Actuators A: Physical*, vol. 108, no. 1-3, pp. 69–74, 2003 (p. 15).

[16] Z. Wang, M. Hong, B. Luk'yanchuk, Y. Lin, Q. Wang and T. Chong, 'Angle effect in laser nanopatterning with particle-mask,' *Journal of Applied Physics*, vol. 96, no. 11, pp. 6845–6850, 2004 (p. 15).

[17] S. I. Kudryashov, A. A. Nastulyavichus, I. N. Saraeva, A. A. Rudenko, D. A. Zayarny and A. A. Ionin, 'Deeply sub-wavelength laser nanopatterning of si surface in dielectric fluids: Manipulation by surface plasmon resonance,' *Applied Surface Science*, vol. 519, p. 146 204, 2020 (p. 15).

[18] A. Kuchmizhak, A. Porfirev, S. Syubaev *et al.*, 'Multi-beam pulsed-laser patterning of plasmonic films using broadband diffractive optical elements,' *Optics letters*, vol. 42, no. 14, pp. 2838–2841, 2017 (p. 15).

[19] A. C. Tam, W. P. Leung, W. Zapka and W. Ziemlich, 'Laser-cleaning techniques for removal of surface particulates,' *Journal of Applied Physics*, vol. 71, no. 7, pp. 3515–3523, 1992 (p. 15).

[20] A. C. Tam, H. K. Park and C. P. Grigoropoulos, 'Laser cleaning of surface contaminants,' *Applied surface science*, vol. 127, pp. 721–725, 1998 (p. 15).

[21] M. N. Ashfold, F. Claeyssens, G. M. Fuge and S. J. Henley, 'Pulsed laser ablation and deposition of thin films,' *Chemical Society Reviews*, vol. 33, no. 1, pp. 23–31, 2004 (p. 15).

[22] A. Vogel and V. Venugopalan, 'Mechanisms of pulsed laser ablation of biological tissues,' *Chemical reviews*, vol. 103, no. 2, pp. 577–644, 2003 (p. 15).

[23] S. Surdo, M. Duocastella and A. Diaspro, 'Nanopatterning with photonic nanojets: Review and perspectives in biomedical research,' *Micromachines*, vol. 12, no. 3, p. 256, 2021 (p. 15).

[24] D. Bäuerle, *Laser processing and chemistry*. Springer Science & Business Media, 2013 (p. 16).

[25] C. Phipps, *Laser ablation and its applications*. Springer, 2007, vol. 129 (p. 15).

[26] B. N. Chichkov, C. Momma, S. Nolte, F. Von Alvensleben and A. Tünnermann, 'Femtosecond, picosecond and nanosecond laser ablation of solids,' *Applied physics A*, vol. 63, no. 2, pp. 109–115, 1996 (p. 16, 17).

[27] A. H. Hamad, *Effects of different laser pulse regimes (nanosecond, picosecond and femtosecond) on the ablation of materials for production of nanoparticles in liquid solution*. IntechOpen London, UK, 2016 (p. 16).

[28] I. Sukhov, G. Shafeev, V. Voronov, M. Sygletou, E. Stratakis and C. Fotakis, 'Generation of nanoparticles of bronze and brass by laser ablation in liquid,' *Applied Surface Science*, vol. 302, pp. 79–82, 2014 (p. 17).

[29] M. S. Brown and C. B. Arnold, 'Fundamentals of laser-material interaction and application to multiscale surface modification,' in *Laser precision microfabrication*, Springer, 2010, pp. 91–120 (p. 17).

[30] B. Jaeggi, B. Neuenschwander, M. Schmid, M. Muralt, J. Zuercher and U. Hunziker, 'Influence of the pulse duration in the ps-regime on the ablation efficiency of metals,' *Physics Procedia*, vol. 12, pp. 164–171, 2011 (p. 17).

[31] J. Krzysztof, *Laser Systems for Applications*. IntechOpen, 2011 (p. 20).

[32] R. Paschotta, 'Active mode locking,' *RP Photonics Encyclopedia,. URL http://www. rp-photonics. com/active_mode_locking. html*, 2017 (p. 20).

[33] U. Keller, K. Weingarten, F. Kartner *et al.*, 'Semiconductor saturable absorber mirrors (sesam's) for femtosecond to nanosecond pulse generation in solid-state lasers,' *IEEE Journal of Selected Topics in Quantum Electronics*, vol. 2, no. 3, pp. 435–453, 1996. DOI: 10.1109/2944.571743 (p. 21).

[34] R. Paschotta, 'Mode locking,' *Encyclopedia of Laser Physics and Technology*, 2011 (p. 21).

[35] H. Nakajima, *Optical Design Using Excel: Practical Calculations for Laser Optical Systems*. John Wiley & Sons, 2015 (p. 22).

[36] E. Abbe, 'Beiträge zur theorie des mikroskops und der mikroskopischen wahrnehmung,' *Archiv für mikroskopische Anatomie*, vol. 9, no. 1, pp. 413–468, 1873 (p. 22).

[37] S. Ram, E. S. Ward and R. J. Ober, 'Beyond rayleigh's criterion: A resolution measure with application to single-molecule microscopy,' *Proceedings of the National Academy of Sciences*, vol. 103, no. 12, pp. 4457–4462, 2006 (p. 24).

[38] T. C. Chong, M. H. Hong and L. P. Shi, 'Laser precision engineering: From microfabrication to nanoprocessing,' *Laser & Photonics Reviews*, vol. 4, no. 1, pp. 123–143, 2010 (p. 25).

[39] S. Sreenivasan, J. Choi, P. Schumaker and F. Xu, 'Status of uv imprint lithography for nanoscale manufacturing,' 2011 (p. 25).

[40] F. Seitz, 'Li schiff, quantum mechanics,' *Bulletin of the American Mathematical Society*, vol. 56, no. 2, pp. 191–192, 1950 (p. 25).

[41] D. Van Labeke, D. Barchiesi and F. Baida, 'Optical characterization of nanosources used in scanning near-field optical microscopy,' *JOSA A*, vol. 12, no. 4, pp. 695–703, 1995 (p. 25).

[42] E. Synge, 'Suggested method for extending microscopic resolution into the ultramicroscopic regime,' *Phil. Mag*, vol. 6, p. 356, 1928 (p. 26).

[43] E. Ash and G. Nicholls, 'Super-resolution aperture scanning microscope,' *Nature*, vol. 237, no. 5357, pp. 510–512, 1972 (p. 26).

[44] E. Betzig, J. K. Trautman, T. Harris, J. Weiner and R. Kostelak, 'Breaking the diffraction barrier: Optical microscopy on a nanometric scale,' *Science*, vol. 251, no. 5000, pp. 1468–1470, 1991 (p. 26).

[45] D. W. Pohl, W. Denk and M. Lanz, 'Optical stethoscopy: Image recording with resolution $\lambda/20$,' *Applied physics letters*, vol. 44, no. 7, pp. 651–653, 1984 (p. 27).

[46] V. G. Veselago, 'The electrodynamics of substances with simultaneously negative values of μ and ε,' *Physics-Uspekhi*, vol. 10, no. 4, pp. 509–514, 1968 (p. 27).

[47] J. B. Pendry, 'Negative refraction makes a perfect lens,' *Physical review letters*, vol. 85, no. 18, p. 3966, 2000 (p. 27).

[48] Y. Lu, L. Zhang, W. Song, Y. Zheng and B. Luk'Yanchuk, 'Laser writing of a subwavelength structure on silicon (100) surfaces with particle-enhanced optical irradi-

ation,' *Journal of Experimental and Theoretical Physics Letters*, vol. 72, no. 9, pp. 457–459, 2000 (p. 28).

[49] Z. Chen, A. Taflove and V. Backman, 'Photonic nanojet enhancement of backscattering of light by nanoparticles: A potential novel visible-light ultramicroscopy technique,' *Optics express*, vol. 12, no. 7, pp. 1214–1220, 2004 (p. 28).

[50] A. Heifetz, S.-C. Kong, A. V. Sahakian, A. Taflove and V. Backman, 'Photonic nanojets,' *Journal of computational and theoretical nanoscience*, vol. 6, no. 9, pp. 1979–1992, 2009 (p. 29).

[51] B. Yan, L. Yue, J. N. Monks *et al.*, 'Superlensing plano-convex-microsphere (pcm) lens for direct laser nano-marking and beyond,' *Optics letters*, vol. 45, no. 5, pp. 1168–1171, 2020 (p. 30).

[52] Q. Wen, X. Wei, P. Zhang, J. Lu, F. Jiang and X. Lu, 'Enhanced microsphere-assisted picosecond laser processing for nanohole fabrication on silicon via thin gold coating,' *Micromachines*, vol. 12, no. 6, p. 611, 2021 (p. 30).

[53] Z. Wang, W. Guo, A. Pena *et al.*, 'Laser micro/nano fabrication in glass with tunable-focus particle lens array,' *Optics Express*, vol. 16, no. 24, pp. 19 706–19 711, 2008 (p. 30).

[54] J.-M. Romano, R. Ahmed, A. Garcia-Giron *et al.*, 'Subwavelength direct laser nanopatterning via microparticle arrays for functionalizing metallic surfaces,' *Journal of Micro and Nano-Manufacturing*, vol. 7, no. 1, 2019 (p. 30).

[55] A. Pena, Z. Wang, D. Whitehead and L. Li, 'Direct writing of micro/nano-scale patterns by means of particle lens arrays scanned by a focused diode pumped nd: Yvo4 laser,' *Applied Physics A*, vol. 101, no. 2, pp. 287–295, 2010 (p. 30, 31).

[56] A. K. S. Kumar, Y. Zhang, D. Li and R. G. Compton, 'A mini-review: How reliable is the drop casting technique?' *Electrochemistry Communications*, vol. 121, p. 106 867, 2020 (p. 32).

[57] M. Dicuangco, S. Dash, J. A. Weibel and S. V. Garimella, 'Effect of superhydrophobic surface morphology on evaporative deposition patterns,' *Applied Physics Letters*, vol. 104, no. 20, p. 201 604, 2014 (p. 32).

[58] D. Tian, Y. Song and L. Jiang, 'Patterning of controllable surface wettability for printing techniques,' *Chemical Society Reviews*, vol. 42, no. 12, pp. 5184–5209, 2013 (p. 32).

[59] X. Ding, P. Li, S.-C. S. Lin *et al.*, 'Surface acoustic wave microfluidics,' *Lab on a Chip*, vol. 13, no. 18, pp. 3626–3649, 2013 (p. 32).

[60] S. Mhatre, A. Zigelman, L. Abezgauz and O. Manor, 'Influence of a propagating megahertz surface acoustic wave on the pattern deposition of solute mass off an evaporating solution,' *Langmuir*, vol. 32, no. 37, pp. 9611–9618, 2016 (p. 32).

[61] T. Ogi, L. B. Modesto-Lopez, F. Iskandar and K. Okuyama, 'Fabrication of a large area monolayer of silica particles on a sapphire substrate by a spin coating method,' *Colloids and Surfaces A: Physicochemical and Engineering Aspects*, vol. 297, no. 1-3, pp. 71–78, 2007 (p. 32, 33, 45).

[62] S. Khanna, P. Marathey, H. Chaliyawala *et al.*, 'Fabrication of long-ranged close-packed monolayer of silica nanospheres by spin coating,' *Colloids and Surfaces A: Physicochemical and Engineering Aspects*, vol. 553, pp. 520–527, 2018 (p. 32, 33, 45).

[63] A. Pockels, 'On the spreading of oil upon water,' *Nature*, vol. 50, no. 1288, pp. 223–224, 1894 (p. 33).

[64] A. Ulman, *An Introduction to Ultrathin Organic Films: From Langmuir–Blodgett to Self–Assembly*. Academic press, 2013 (p. 33).

[65] S. Acharya, A. B. Panda, N. Belman, S. Efrima and Y. Golan, 'A semiconductor-nanowire assembly of ultrahigh junction density by the langmuir–blodgett technique,' *Advanced Materials*, vol. 18, no. 2, pp. 210–213, 2006 (p. 33).

[66] Z. Matharu, G. Sumana, S. K. Arya, S. Singh, V. Gupta and B. Malhotra, 'Polyaniline langmuir- blodgett film based cholesterol biosensor,' *Langmuir*, vol. 23, no. 26, pp. 13 188–13 192, 2007 (p. 33).

[67] K. Ramanathan, M. Ram, B. Malhotra and A. S. N. Murthy, 'Application of polyaniline-langmuir-blodgett films as a glucose biosensor,' *Materials Science and Engineering: C*, vol. 3, no. 3-4, pp. 159–163, 1995 (p. 33).

[68] V. Periasamy, M. M. Jaafar, K. Chandrasekaran *et al.*, 'Langmuir–blodgett graphene-based films for algal biophotovoltaic fuel cells,' *Nanomaterials*, vol. 12, no. 5, p. 840, 2022 (p. 33).

[69] D. K. Schwartz, 'Langmuir-blodgett film structure,' *Surface Science Reports*, vol. 27, no. 7-8, pp. 245–334, 1997 (p. 34).

[70] M. Evyapan, A. K. Hassan and A. Dunbar, 'Understanding the gas adsorption kinetics of langmuir-schaefer porphyrin films using two comparative sensing systems,' *Sensors and Actuators B: Chemical*, vol. 254, pp. 669–680, 2018 (p. 34).

[71] K. Lambert, R. K. Capek, M. I. Bodnarchuk *et al.*, 'Langmuir- schaefer deposition of quantum dot multilayers,' *Langmuir*, vol. 26, no. 11, pp. 7732–7736, 2010 (p. 34).

[72] Bangs Laboratories Inc., 'Tech notes 203A - Drying and re-suspending microspheres,' 2013 (p. 42).

[73] ——, 'Tech notes 202 - Preventing aggregation microspheres,' 2013 (p. 43).

[74] G. M. Ong, A. Gallegos and J. Wu, 'Modeling surface charge regulation of colloidal particles in aqueous solutions,' *Langmuir*, vol. 36, no. 40, pp. 11 918–11 928, 2020 (p. 43).

[75] T. Tadros, 'Electrostatic repulsion and colloid stability,' *Encyclopedia of Colloid and Interface Science*, pp. 363–363, 2013 (p. 43).

[76] B. TechNote, '201,"working with microspheres",© 2002, bangs laboratories,' *Inc.(20 Pages)*, (p. 44).

[77] J. Hruby, V. T. Santana, D. Kostiuk *et al.*, 'A graphene-based hybrid material with quantum bits prepared by the double langmuir–schaefer method,' *Rsc Advances*, vol. 9, no. 42, pp. 24 066–24 073, 2019 (p. 46, 47).

[78] V. Lotito and T. Zambelli, 'Self-assembly of single-sized and binary colloidal particles at air/water interface by surface confinement and water discharge,' *Langmuir*, vol. 32, no. 37, pp. 9582–9590, 2016 (p. 46, 48).

[79] J. G. Speight, *Natural water remediation: Chemistry and technology*. Butterworth-Heinemann, 2019 (p. 46).

[80] M. J. Large, S. P. Ogilvie, A. A. King and A. B. Dalton, 'Understanding solvent spreading for langmuir deposition of nanomaterial films: A hansen solubility parameter approach,' *Langmuir*, vol. 33, no. 51, pp. 14 766–14 771, 2017 (p. 49).

[81] R. A. L. Jones, R. A. Jones, R. Jones *et al.*, *Soft condensed matter*. Oxford University Press, 2002, vol. 6 (p. 49).

[82] A. S. Budi, R. D. Mayasari, A. E. Mulyono *et al.*, 'Observation of chemicals evaporation (ethanol, methanol and 2-propanol) using vibrated microcantilever,' in *AIP Conference Proceedings*, AIP Publishing LLC, vol. 2331, 2021, p. 030 007 (p. 49).

[83] D. Nieto, J. Arines, G. M. O'Connor and M. T. Flores-Arias, 'Single-pulse laser ablation threshold of borosilicate, fused silica, sapphire, and soda-lime glass for pulse widths of 500 fs, 10 ps, 20 ns,' *Applied optics*, vol. 54, no. 29, pp. 8596–8601, 2015 (p. 50).

[84] G. Wang, C. Lopez-Molina and B. De Baets, 'Automated blob detection using iterative laplacian of gaussian filtering and unilateral second-order gaussian kernels,' *Digital Signal Processing*, vol. 96, p. 102 592, 2020 (p. 54).

[85] nanoComposix, *Depositing monolayers and thin films of nanoparticles*. [Online]. Available: `https://nanocomposix.com/pages/depositing-monolayers-and-thin-films-of-nanoparticles` (p. 60).

[86] A. Nikolov and D. Wasan, 'Wetting–dewetting films: The role of structural forces,' *Advances in Colloid and Interface Science*, vol. 206, pp. 207–221, 2014 (p. 60).

[87] D. T. Toolan, S. Fujii, S. J. Ebbens, Y. Nakamura and J. R. Howse, 'On the mechanisms of colloidal self-assembly during spin-coating,' *Soft Matter*, vol. 10, no. 44, pp. 8804–8812, 2014 (p. 61).

[88] W. Zengbo, 'Optical resonance and near field effects: Small particles under laser irradiation,' 2005 (p. 68).